Optoelectronic properties of high pressure regulated transition metal dichalcogenides and their heterostructures*

LI Chenkai[1], ZHU Jinlong[1,2,3]

1. Department of Physics, State key laboratory of quantum functional materials, and Guangdong Basic Research Center of Excellence for Quantum Science, Southern University of Science and Technology (SUSTech), Shenzhen 518055, China

2.Quantum Science Center of Guangdong-Hong Kong-Macao Greater Bay Area (Guangdong), Shenzhen 518045, China

3. Institute of Major Scientific Facilities for New Materials, Southern University of Science and Technology, Shenzhen 518055, China

Abstract

Semiconducting transition metal dichalcogenides exhibit layer-dependent bandgaps, strong excitonic effects, and spin-valley coupling, positioning them as promising candidates for optoelectronic applications. In heterostructures formed by van der Waals stacking, interlayer excitons and moiré superlattices have emerged as a unique platform for exploring quantum many-body physics and correlated electronic phases. Applying high pressure to semiconducting transition metal dichalcogenides and their heterostructures enables precise and continuous tuning of their optoelectronic properties via anisotropic lattice compression, particularly the dramatic reduction of interlayer distances, which greatly enhances interlayer orbital hybridization over traditional tuning methods. This review systematically presents diamond anvil cell techniques for *in situ* high-pressure characterization and analyzes the pressure-induced evolution in semiconducting transition metal dichalcogenides and their heterostructures. It focuses on four key aspects: 1) Atomic-scale structural phase transitions (e.g., layer sliding) and corresponding electronic band structure modifications, including direct-to-indirect bandgap transitions in monolayers (*K*-Λ crossover) and metallization/superconductivity; 2) Quantifiable enhancement of interlayer interactions revealed by layer-dependent phonon shifts and spin-orbit splitting amplification, along with the mechanisms of their influence on properties; 3) Modulation of exciton binding states and related mechanisms, covering intralayer excitons, trions and interlayer excitons; 4) Moiré potential modulation where high pressure significantly deepens potentials via interlayer

---

* The paper is an English translated version of the original Chinese paper published in Acta Physica Sinica. Please cite the paper as: **LI Chenkai, ZHU Jinlong, Optoelectronic properties of high pressure regulated transition metal chalcogenides and their heterostructures.** *Acta Phys. Sin.*, 2025, 74(17): 176802. DOI: 10.7498/aps.74.20250498

compression. This review particularly highlights the unique capability of high pressure in enhancing interlayer orbital hybridization, thereby inducing exotic quantum phases. Finally, the future research directions in this field are outlined to advance quantum information device design, strongly correlated electron system simulation, and the novel excitonic state exploration.

Keywords: high pressure, transition metal dichalcogenides, exciton, Moiré superlattices

PACS：62.50.-p,73.21.Cd, 68.65.-k

doi: 10.7498/aps.74.20250498

cstr: 32037.14.aps.74. 20250498

1. Introduction

Since the successful exfoliation of graphene in 2004 [1], two-dimensional (2D) materials have rapidly become one of the important research directions in the fields of materials, physics and chemistry. Graphene has garnered significant research interest due to its exceptional physical properties, such as high electron mobility[1–4], near full-band high transmittance[5], high mechanical strength[6,7], Mott-insulating and superconducting phase[8,9] under magic twist angle, and a large number of achievements have been made in both basic research and application. However, the semi-metallic nature of graphene and its near-zero band gap limit its application in optoelectronic devices. As researchers further expand the 2D materials, more kinds of 2D materials have been discovered, such as phosphorene[10,11], silicene[12–14], boron nitride[15–18], transition metal dichalcogenides (TMD)[19–22], etc. The chemical formula of the TMD material is MX_2, wherein M is a transition metal group element (Mo or W, etc.), and X is a chalcogen group element (S, Se or Te, etc.). Its constituent elements and crystal structures are diverse (such as 2H, 1T, 1T'), as shown by Fig. 1(a)-(b), which makes TMD materials show rich physical properties, such as strong light-matter interaction, charge density wave, superconductivity, topological properties, etc[23,24]. In this paper, we mainly discuss the 2H phases MoS_2, WS_2, $MoSe_2$ and WSe_2, which are semiconductors and have layer-dependent visible band gaps, compensating for graphene's limitations in optoelectronic applications while maintaining excellent environmental stability[25,26]. In addition, due to the weak interlayer van der Waals interaction of TMD materials, their monolayers can be stacked vertically at will to form heterostructures, as shown in Fig. 1(c)[27].

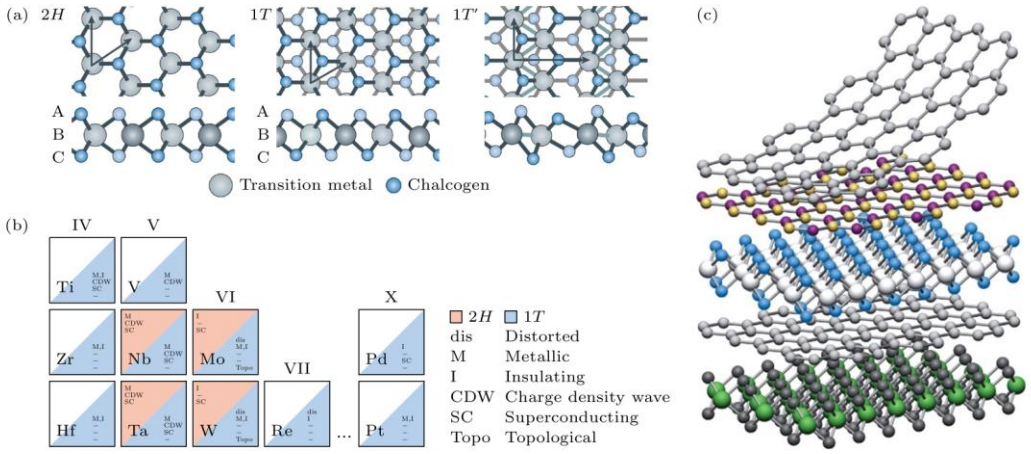

Figure 1. (a) Atomic structure of monolayer of TMDs in their trigonal prismatic (2*H*), distorted octahedral (1*T*) and dimerized (1*T*′) phases[24]; (b)"periodic table" of known layered TMDs, organized based on the transition metal element involved, summarizing their existing structural phases and indicating the presence of distorted structural phases and observed electronic phases[24]; (c) schematic diagram of building van der Waals heterostructures[27].

It is worth noting that in the monolayer, the enhanced Coulomb interaction due to the reduced screening gives rise to tight-binding excitons with strong light-matter interaction. The strong Coulomb interaction also favors the generation of multiparticle exciton complexes. Excitons combine or interact with other particles or quasi-particles such as excitons, electrons (holes) or phonons, resulting in exciton complexes such as biexcitons, trions, exciton-trion complexes and dark exciton phonon replicas [28]. In exciton complexes, unique physical properties may emerge, which may be used for new exciton state engineering. Moreover, by revealing the interaction between excitons and various quasiparticles, the basic laws of quantum many-body physics can be further clarified [28–31]. At the same time, the large spin-orbit coupling and the unique valley spin provide the conditions for the dynamic manipulation of the valley degree of freedom. In addition, the electric dipole interaction between interlayer excitons and the periodic Moiré pattern in the heterostructure become an effective platform for the emergence of exciton states, including localized exciton states, new optical selection rules, and the realization of correlated physical phenomena, such as Mott insulator, Wigner crystal and unconventional superconductivity, which are manifested in the new generation of optoelectronic devices and quantum simulation[28,29,32–39].

To sum up, TMD shows great potential in the fields of optoelectronics and quantum information because of its strong exciton effect, intrinsic valley spin polarization and easy construction of van der Waals heterostructure. Gate voltage, as a powerful means to control the carrier concentration in thin films, can be used to control the exciton state, metallization and superconducting state, as well as the related states in Moiré superlattice, but its impact on the intrinsic properties of materials such as band dispersion and interlayer coupling strength is

limited. Although the stacking/twist angle can regulate the interlayer interaction and Moiré potential, its regulation range and continuity are limited, and disorder may be introduced. Although the strain control applied by the substrate can achieve continuous control of the electronic structure, it is non-hydrostatic and local, and the amount of strain that can be applied is limited. In contrast, high pressure provides a unique, clean, and powerful regulatory pathway. Its core advantage is that it can continuously compress the lattice in a large range, especially significantly reduce the interlayer distance dominated by weak van der Waals force, thus efficiently enhancing the interlayer interaction. The interlayer interaction is the key factor to determine the photoelectric properties of TMD, which is also difficult to achieve by other methods [40]. In addition, high pressure can induce the phase transition of crystal structure and electronic structure to produce new states[21,41–52]. Therefore, by revealing the evolution of optoelectronic properties of TMD under high pressure, it provides a powerful platform for in-depth understanding of basic scientific issues such as interlayer interaction, phase transition mechanism, and many-body interaction, and opens up a new way to explore the design principles of high-performance optoelectronic devices and quantum simulation platforms under extreme conditions.

At present, the research on the high pressure control of the photoelectric properties of semiconductor TMD and its heterostructure mainly focuses on the following four core scientific issues: 1) the evolution and phase transition of crystal structure and electronic structure under high pressure, focusing on the revelation of various phase transition mechanisms and the generation of novel physical properties, such as superconductivity; 2) The enhancement of interlayer interaction under compression and its influence mechanism. By comparing the evolution of samples with different layers under high pressure, the relationship between interlayer interaction and pressure and the number of layers can be quantitatively established, and the specific mechanism of its physical property control (especially different from the in-plane compression effect) can be clarified; 3) The many-body interaction mechanism in exciton complexes, exploring how high pressure finely regulates exciton binding energy, lifetime, valley polarization and other characteristics, and revealing the many-body interaction mechanism between excitons and various particles/quasi-particles; 4) The exploration of strongly correlated states in the Moiré potential, quantifying the effect of high pressure enhanced interlayer interaction on the depth of the Moiré potential, and revealing the thermal stability enhancement of potential strongly correlated states and the emergence of new correlated states after the deepening of the Moir potential. The overall core goal is to reveal and design rich physical phenomena in materials by precisely manipulating the interaction between TMD and heterostructure under high pressure, especially the key parameter of interlayer coupling.

In this paper, the experimental research progress of semiconductor TMD and its

heterostructure under high pressure is systematically summarized, focusing on the changes of physical properties such as structural phase transition, electronic state control, exciton behavior evolution and Moiré potential control induced by high pressure, in order to reveal the unique role of high pressure in enhancing interlayer coupling and inducing novel states, and to look forward to the future direction of multi-field control. First, high-pressure technology will be briefly introduced in Section2; After that, the behavior of TMD and heterostructure under high pressure is discussed in Section3 and Section4 in turn; Finally, the paper summarizes and looks forward to the potential directions in the future exploration of basic physics and the design of functional devices in this field, which provides a new perspective for the study of extreme conditions of two-dimensional materials.

2. High-pressure technique

The diamond anvil cell (DAC) is the most widely used device for in situ high-pressure optoelectronic characterization, and its device is shown in Fig. 2(a). DACs made of different materials can be selected according to different test targets. For example, stainless steel DAC is mainly used for normal temperature test, while beryllium copper DAC with good thermal conductivity and non-magnetic material is used for photoelectric test at low temperature/magnetic field. The key part of the DAC is a pair of diamonds, which are pressed against each other to generate high pressure. The ultra-high hardness of diamond enables it to withstand high pressure. The diamond anvil culet is available in various sizes, ranging from tens of microns to several millimeters. The smaller the size, the higher the maximum pressure that can be generated. A typical diamond with a diameter of 300 μm can produce a maximum pressure of about 50-60 GPa. A static high pressure of more than 400 GPa can be generated in the sample cavity of the DAC, which is much higher than the pressure at the center of the earth (about 360 GPa) [53]. Importantly, the weak absorption of diamond in a wide range of wavelengths facilitates the transmission of both probe and sample signal light, allowing DAC to be used for most optoelectronic characterizations. Its insulation makes it possible to place electrodes or plated electrodes on the diamond for in situ electrical transport measurement of the sample in the cavity.

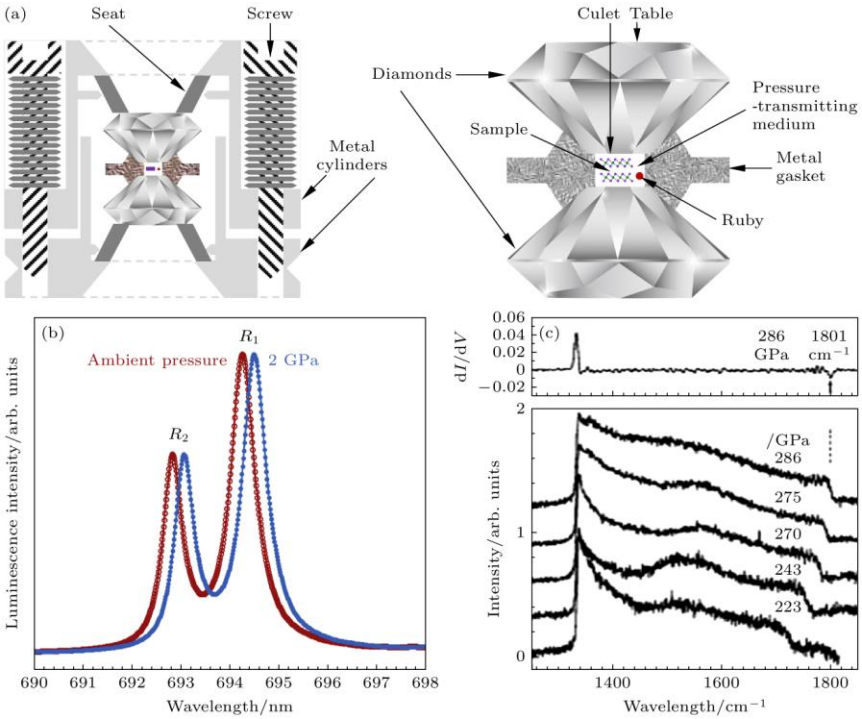

Figure 2. (a) Schematic illustration of the cross-section of a DAC (left) , and the zoom-in on the diamond/gasket assembly (right)[40]; (b) illustration of the shift in position of the R1 fluorescence line of ruby on increasing pressure from ambient pressure to 2 GPa at room temperature[54]; (c) (top) typical Raman spectra from the center of the diamond anvil culet at various pressures in 223–286 GPa range and (bottom) the differential spectrum at 286 GPa, the high-frequency edge of the Raman band was defined as a minimum of the differential[55].

Another common pressurization device is the piston-cylinder pressure cell, which is often used for cryogenic electrical measurement [56–58]. Compared with the diamond anvil cell, the piston-cylinder pressure cell has better hydrostatic pressure conditions and a larger sample cavity, which can accommodate samples of mm size. This is particularly conducive to the high-pressure experiments of complex electrical devices: by cutting devices on silicon wafers into small sizes and directly putting them into high-pressure cavities, the difficulty of micro-nano fabrication on small size (< 500 μm) diamond is avoided[56,57]. It is worth noting that the piston-cylinder pressure cell has some limitations, such as the small maximum pressure (less than about 3 GPa), which limits the control range of physical properties, and the lack of optical window, which limits the optical test. Because of these limitations, the current research on semiconductor TMD and its heterostructure has not been applied to piston-cylinder cell. However, the advantages of electrical device testing will be beneficial to the application of related high-pressure research in the future, which will be discussed in the last part.

The pressure is usually calibrated by the peak position of the R1 photoluminescence (PL)

peak of Ruby (Cr^+-doped Al_2O_3) and the peak position of the high frequency edge of the diamond Raman peak. Among them, the ruby fluorescence pressure gauge is suitable for a wide range of pressure environments (about 0-60 GPa), and the pressure is calibrated according to the shift of the fluorescence R1 peak position at high pressure, as shown in the Fig. 2(b). The specific formula of ruby scale is: $P[\mathrm{GPa}] = 1.87(\pm 0.01) \times 10^3 (\frac{\Delta\lambda}{\lambda_0}) \times [1 + 5.63(\pm 0.03)(\frac{\Delta\lambda}{\lambda_0})]$, where P is the current pressure, and $\Delta\lambda$ is the difference between the fluorescence peak wavelength of ruby R1 at the current pressure and the fluorescence peak wavelength λ_0 (~ 694.25 nm) at ambient pressure[59]. The pressure gauge using diamond Raman is suitable for pressure calibration between 20-300 GPa, as shown in Fig. 2(c). The high frequency edge is defined as the minimum of the first differential of the Raman intensity. The corresponding standard pressure formula is $P[\mathrm{GPa}] = 547(\pm 11) \times (\frac{\Delta\nu}{\nu_0})[(1.37 \pm 0.1)(\frac{\Delta\nu}{\nu_0})]$, where $\Delta\nu$ is the difference between the Raman shift at the edge of Raman peak under pressure and at ambient pressure ν_0 (about 1334 cm^{-1})[55]. Note that the above two formulas are only applicable to room temperature conditions. In high or low temperature experiments, the temperature shift of λ_0 and ν_0 values should be taken into account, and the fitting formulas should be slightly modified [60–63].

3. TMD under high pressure.

3.1 Crystal structure evolution

Semiconductor TMD materials generally have a $2H_c$ structure at ambient pressure, as shown in the Fig. 3(a). Under high pressure, the lattice of $2H_c$-TMD is compressed, which is reflected by the decrease of lattice constant measured by X-ray diffraction (XRD) and the blue shift of Raman peak. Taking WSe_2 as an example, as shown in Fig. 3(b)-(d), the blue shift of Raman peaks results from an increase in phonon frequency due to enhanced interatomic forces under compression. With the increase of pressure, the structural phase transformation of $2H_c$-$2H_a$ occurs in the bulk. The $2H_a$ structure is shown in Fig. 3(a), which is formed by interlayer sliding of the $2H_c$ structure. The phase transition can be revealed by the discontinuous change in the lattice constant and the Raman peak splitting or jumping, which is shown by Fig. 3(b)-(d) using WSe_2 as an example. The phase transformation usually occurs in a wide pressure range, that is, from the beginning to the end of the phase transformation. In this range, the interlayer sliding proceeds gradually, and the peak splitting often persists in XRD or Raman spectra, as shown by Fig. 3(b)-(d)[42,45,64,65]. The phase transition pressures vary among different materials. For bulk $MoSe_2$, WS_2 and WSe_2, they are 20-40 (beginning to complete phase transformation)[42], 15-45[65] and 28.5-60 GPa[64], respectively. For bulk $MoSe_2$, it is considered that $2H_c$ phase remains at about 60 GPa. The

difference of pressure points of phase transformation is considered to be caused by the different phase transformation barriers[66].

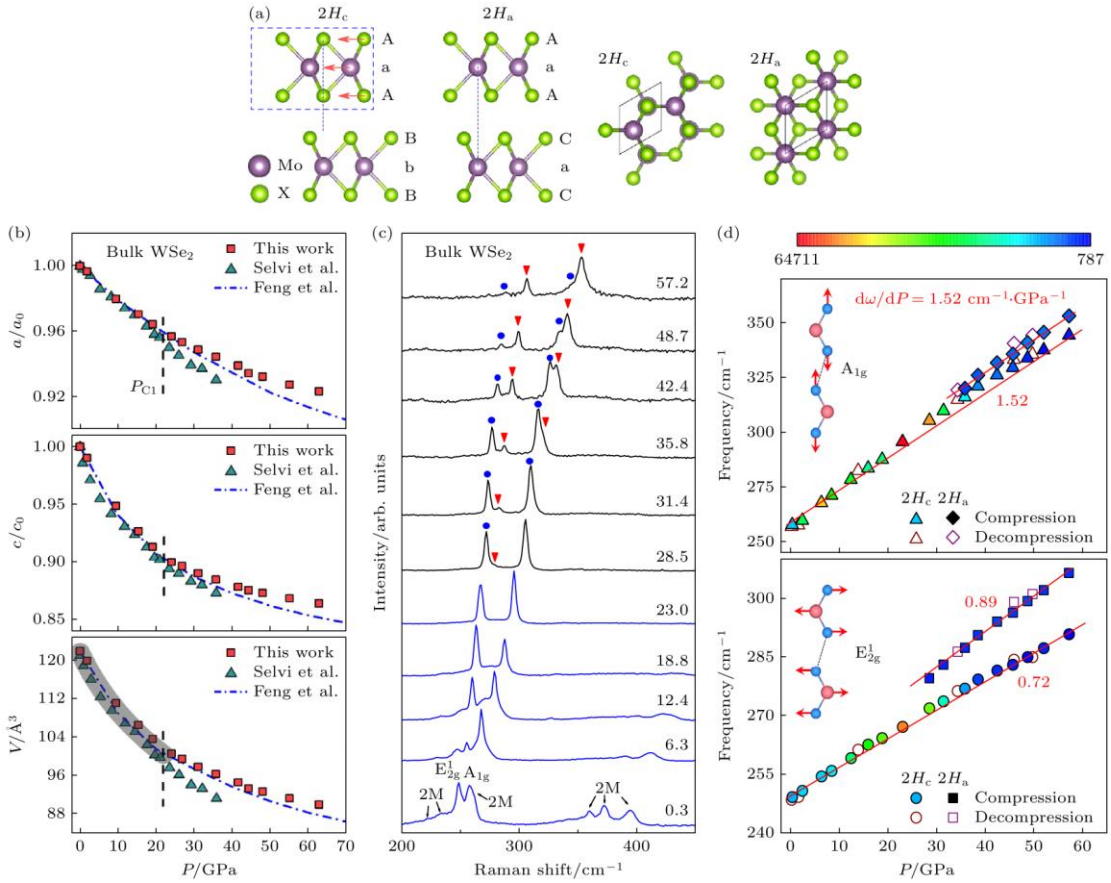

Figure 3. (a) The side view (projected on *ac* plane) and top view (projected on *ab* plane) of $2H_c$ and $2H_a$ structure in MX_2, *M* represents Mo and W, *X* represents S and Se, the red arrows represent one sliding path for the $2H_c$ to $2H_a$ transition, where one unit of *X*-*M*-*X* triple layers (marked by a blue box) shifts in ab plane[66]; (b) the normalized cell parameters a/a_0, c/c_0, and the volume *V* of WSe_2 as a function of pressure[64]; (c) room temperature Raman spectra of WSe_2 in the compression[64]; (d) peak frequencies of A_{1g} and E^1_{2g} modes as a function of pressure of WSe_2, respectively, inset shows scheme of the Raman modes A_{1g} and E^1_{2g}[64].

Layer number dependence, as one of the important properties in layered materials, controls material properties by changing the interaction between layers. According to the Raman spectra of samples with different number of layers, the layer-dependent structural characteristics can be revealed. Specifically, at ambient pressure, with the decrease of the number of layers, the in-plane vibration mode E^1_{2g} will be blue-shifted, while the out-of-plane vibration mode A_{1g} will be red-shifted, as shown in Fig. 4(a)-(b) using MoS_2 as an example[67]. Among them, the blue shift of E^1_{2g} is due to the decrease of charge screening with the decrease of layer number, which leads to the increase of long-range Coulomb interaction between effective charges, thus increasing the restoring force. The red shift of A_{1g}

is due to the weakening of interlayer binding force[46,67–69]. In addition, the response of Raman modes at high pressure, such as the blue-shift rate, is also layer-dependent. In MoS_2 and WS_2, the blue shift rate of E^1_{2g} mode in monolayer is higher than that in bilayer, but the rate of A_{1g} mode is lower. By comparing the cases with and without interlayer interaction (bilayer and monolayer), the presence of interlayer interaction makes the out-of-plane compression more sensitive to external pressure, while the in-plane compression is the opposite[70,71]. This trend is also found in multilayer (2-layer to bulk) MoS_2, that is, with the increase of the number of layers *N*, the blue shift rate of E^1_{2g} mode decreases, while the blue shift rate of A_{1g} mode increases, as shown in Fig. 4(c)[72]. In the diatomic chain model (DCM), the shear force constant C^S_b between sulfur planes in adjacent layers and the shear force constant C^S_w between molybdenum and sulfur planes in the same layer are fitted based on the experimental data under high pressure, and the ratio C^S_b/C^S_w characterizes the relative strength of interlayer and intralayer interactions, with larger values indicating stronger interlayer coupling[72,73]. Based on this ratio, it is quantitatively revealed that the larger the number of layers is, the stronger the interlayer interaction is. And the interlayer interaction increases with the increase of pressure. And the degree of pressure-induced enhancement of interlayer interaction is positively correlated with the number of layers, as shown by Fig. 4(d)[72].

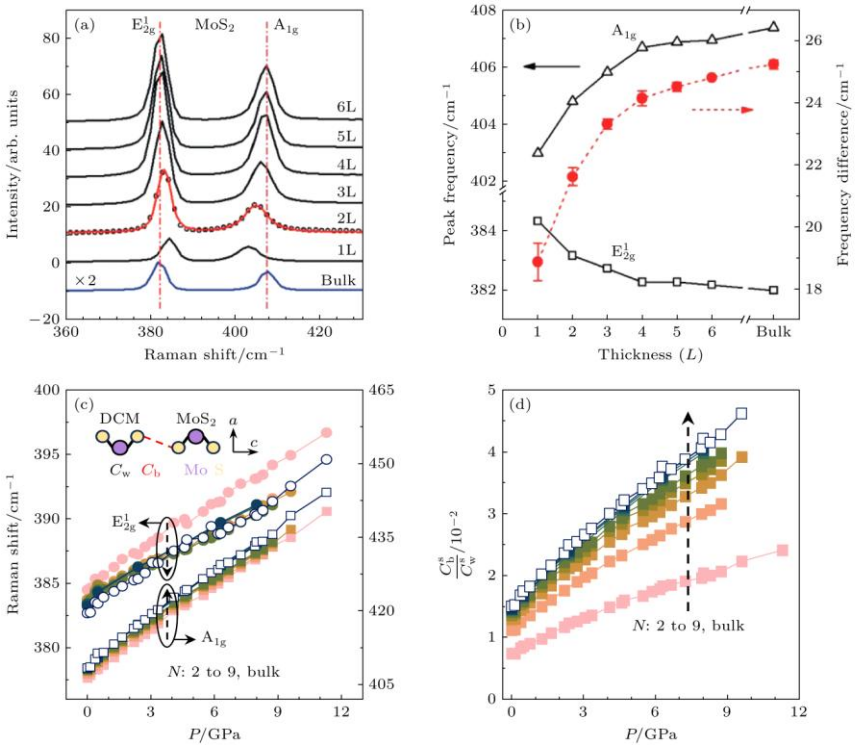

Figure 4. (a) Raman spectra of thin and bulk MoS_2 films[67]; (b) frequencies of E^1_{2g} and A_{1g} Raman modes (left vertical axis) and their difference (right vertical axis) as a function of layer thickness[67]; (c) pressure-dependence of Raman shift of A_{1g} and E^1_{2g} with various *N*, and *N* changed from 2 to 9, and bulk, inset shows the DCM of MoS_2[72]; (d) pressure-dependence of C^S_b/C^S_w with various *N*[72].

The low-frequency interlayer vibrational modes include the interlayer breathing (LB) and shear (S) modes, as illustrated in Fig. 5(a). The former corresponds to the synchronous expansion and contraction vibrations between adjacent layers along the vertical direction (*z*-direction), resembling the breathing motion of a spring. The latter corresponds to the relative sliding vibrations between adjacent layers along the in-plane direction (*xy*-direction). The interlayer vibration mode is absent in the monolayer due to the lack of adjacent layers. The restoring force of the interlayer vibration modes is dominated only by the interlayer van der Waals interaction, so they are very sensitive to the interlayer interaction, which provides a powerful probe to explore the evolution of the interlayer interaction with the number of layers and pressure. As shown in the Fig. 5(b), the monoatomic chain model (MCM) is formed by simplifying each layer as a rigid sphere and assuming that each layer and its adjacent layers vibrate rigidly. The model can effectively explain the layer number dependence of the interlayer vibration mode at ambient and high pressures[72,74,75]. The TMD of the *N* layer usually includes (*N* – 1) twice-degenerate S modes and (*N* – 1) non-degenerate LB modes, and the frequencies are:

$\omega(S_{N,N-j}) = \omega(S_{\text{bulk}})\sin(j\pi/2N), \omega(\text{LB}_{N,N-j}) = \omega(\text{LB}_{\text{bulk}})\sin(j\pi/2N)$, where $\omega(S_{\text{bulk}}) = \frac{1}{\pi c}\sqrt{\frac{\alpha^{//}}{\mu}}, \omega(\text{LB}_{\text{bulk}}) = \frac{1}{\pi c}\sqrt{\frac{\alpha^{\perp}}{\mu}}$ is the frequency of the corresponding phonon in the bulk, the phonon branching coefficient j = 1, 2, 3, $\cdots$; $N-1$, $\alpha^{//}$ and $\alpha^{\perp}$ are the interlayer force constants per unit area of the in-plane and out-of-plane nearest-neighbor layers, respectively, μ is the mass per unit area of each layer, and c is the speed of light [72,74,75]. Experimentally, it is easy to observe the highest frequency S-mode branch ($j = N-1$, i.e. E^2_{2g}) and the lowest frequency LM-mode branch (j = 1, i.e. B_{2g}), as shown by Fig. 5(c)-(d)[72]. According to this model, it is easy to obtain the layer number dependence of the frequency: with the increase of the layer number, the $S_{N,1}$ is blue-shifted and the $\text{LB}_{N,N-1}$ is red-shifted, and the layer number dependence can be well fitted by the MCM model, as shown by Fig. 5(c)-(d)[72]. At high pressure, both LM and S modes show blue shift due to lattice compression, and the blue shift rate shows layer number dependence, as shown by Fig. 5(e)[72]. According to the MCM model, the blue shift rates are $\frac{d\omega(S_{N,1})}{dP} = \frac{d\omega(S_{\text{bulk}})}{dP}\sin\frac{\pi(N-1)}{2N}, \frac{d\omega(\text{LB}_{N,N-1})}{dP} = \frac{d\omega(\text{LB}_{\text{bulk}})}{dP}\sin\frac{\pi}{2N}$. With the increase of layer number *N*, the former increases and the latter decreases. It is noted that the $\alpha^{\perp}$ increases faster with pressure than the $\alpha^{//}$ because the interlayer compression is more sensitive to pressure regulation, which results in a larger blue shift rate of the $\text{LB}_{2,1}$ mode with pressure in the case of N = 2. When N tends to infinity, the blue shift rate of $\text{LB}_{N,N-1}$ tends to zero, which is less than the finite value of S-mode. As a result, the blue shift rates of $\text{LB}_{N,N-1}$ and $S_{N,1}$ modes must have a crossover point with the number of layers, which is 4 layers in MoS_2, as shown in Fig. 5(e), and 3 layers in $MoTe_2$[72,74]. To sum up, the layer number and pressure dependence of the interlayer vibration mode of 2*H*-TMD can be completely described by the

MCM model, and the details of the evolution behavior with layer number or pressure are determined only by the element type, force constants $\alpha^{\perp}$ and $\alpha^{//}$, and their evolution with pressure.

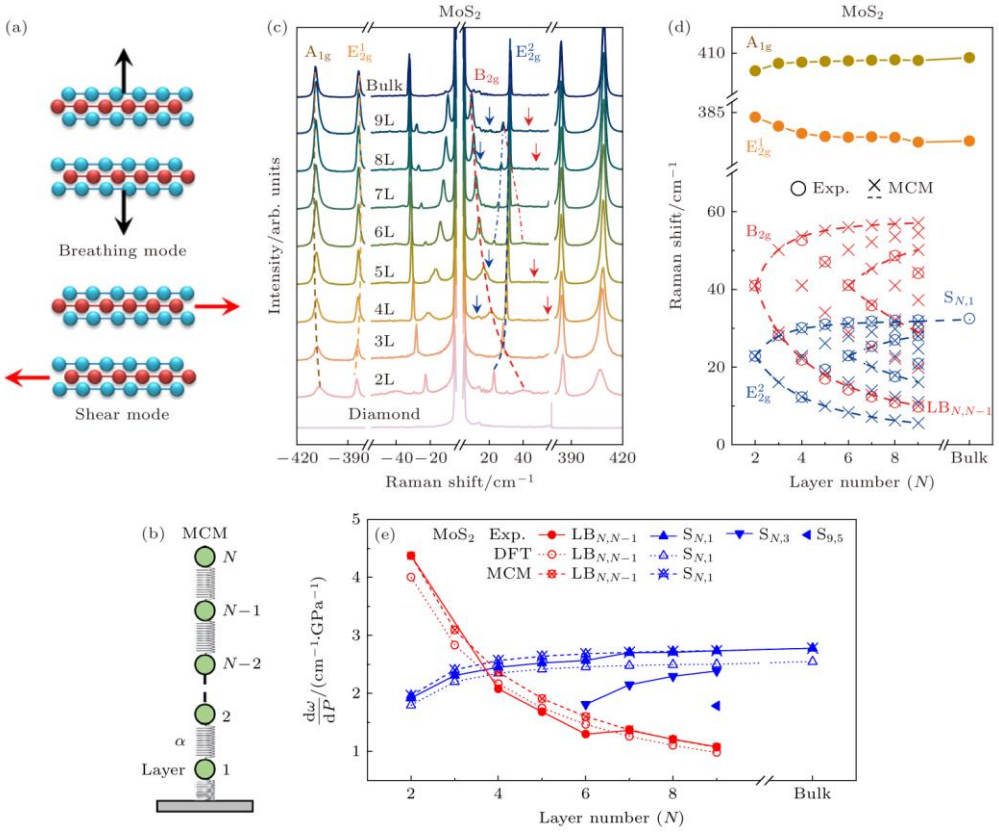

Figure 5. (a) Schematics of interlayer breathing mode and shear mode[76]; (b) MCM of MoS_2 on a solid substrate[72]; (c) Stokes and anti-Stokes Raman spectra of the few-layer and bulk MoS_2 on a diamond surface, the dashed lines and arrows are used for guide[72]; (d) Raman shifts of few-layer MoS_2 as a function of N[72]; (e) N-dependence of Raman shifting rates of LB and S of MoS_2[72].

The pressure-induced $2H_c$-$2H_a$ structural phase transition also exhibits a layer-number dependence, such as the transition pressure. In general, it is believed that the smaller the number of layers in a layered material, the higher the phase transition pressure required, which is due to the layer-number dependence of the surface energy[77]. However, the results in TMD are different. At present, interlayer sliding is found in bilayer MoS_2 and bilayer WS_2 through the jump of Raman peaks, at about 16[70] and about 15 GPa[71], respectively, which are lower than the transition pressures of bulk and multilayer reported by the same report or previous reports[42,65,70,71]. According to the study[72] of few-layer MoS_2, the interlayer shear constant C_b^S is positively correlated with the number of layers, which reveals that the interlayer restoring force decreases with the decrease of the number of layers, thus providing a possible reason for the easier occurrence of interlayer sliding under high pressure. In the

monolayer, there is a lack of phase transition of interlayer sliding due to the absence of adjacent layers, and it is believed that no structural phase transition is found under hydrostatic pressure below about 40 GPa[41,70,71].

It is worth noting that for monolayer or few layers, the structural properties are susceptible to pressure environments, such as hydrostatic conditions and substrate effects. In some experiments, the thin film sample is placed in a high-pressure cell together with a silicon wafer or other substrate[46,78]. Due to the difference of compression deformation between the pressure transmitting medium and the substrate under high pressure, the stress on the upper and lower surfaces of the sample is different. This difference introduces additional stresses, which in turn cause structural distortion. For example, in monolayer MoS_2, due to the different stress environments of the upper and lower Mo-S bonds, the Raman peaks are split, and further, new peaks[46] appear due to the structural distortion. the large volume collapse of the silicon wafer during phase transition under high pressure causes all the Raman peaks of monolayer WS_2 to soften and jump[78]. It is generally believed that when a monolayer or few layers of material are transferred directly to the diamond anvil surface, the interaction between the diamond and the sample is weak enough to effectively avoid the problem of different stress conditions between the upper and lower surfaces of the sample[41,70,71,78]. In addition, under different hydrostatic pressure conditions, which is determined by the pressure transmitting medium, the response of the sample to compression is also different, which is manifested by the difference in the blue shift rate of the Raman peak[70,71].

3.2 Electronic structure evolution

Bulk TMDs exhibit a gradual reduction of their band gap under high pressure, leading to a metallization phase transition. In MoS_2, WS_2, and WSe_2, this semiconductor-to-metal transition typically accompanies the structural transformation, as exemplified by MoS_2 in Fig. 6 [42,64,65]. For $MoSe_2$, which lacks a structural phase transition, metallization also occurs, again due to a pressure-induced band gap closing at about 41 GPa [66]. More notably, superconductivity in $2H_a$-MoS_2 occurs after further pressurization above about 90 GPa, which is believed to be related to the pressure-induced emergence of new flat Fermi pockets [79].

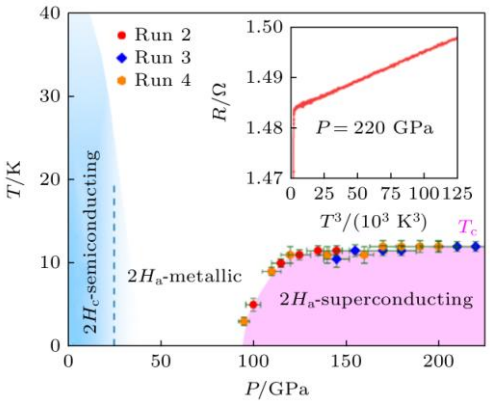

Figure 6. Pressure-temperature (*P*-*T*) phase diagram of 2*H*-MoS_2[79].

The electronic structure also has a significant layer number dependence. The bulk material is an indirect band gap semiconductor, usually the valence band maximum (VBM) is at the *Γ* point, and the conduction band minimum (CBM) is at the *M* point between *K* and *Γ*, as shown in Fig. 7(a), with a band gap of about 1 eV. When the number of layers is reduced to a monolayer, it changes from an indirect band gap semiconductor to a *K*-*K* direct band gap semiconductor with a band gap of about 2 eV[19,80,81]. As shown in Fig. 7(b), taking MoS_2 as an example, in few-layer materials, PL peak I corresponds to indirect transition, PL peaks A and B correspond to *K*-*K* direct transition, and the energy splitting is attributed to the spin-orbit coupling splitting of the valence band. The indirect transition peak I disappears and the intensity of peak A increases greatly due to the indirect-direct band gap phase transition from bilayer to monolayer. The layer number dependent indirect to direct band gap phase transition is mainly caused by the orbital characteristics of different points. The *K* point electronic state involves only the strongly localized *d*-orbital hybridization of the metal atoms located in the middle of the monolayer, and thus has weak interlayer coupling. The electronic states at the *Λ* point of the conduction band and the *Γ* point of the valence band are both involved in the hybridization of the *d* orbital of the metal atom and the p_z orbital of the chalcogen atom, and are more easily affected by the interlayer coupling[82]. With the decrease of the layer number, the *Λ*-*Γ* gap increases, while the *K*-*K* gap is almost unchanged, resulting in the change of the VBM from *Γ* to *K* and the CBM from *Λ* to *K*. In a bilayer, the VBM is generally *Γ*, and the CBM may be *K* or *Λ*, as shown by Fig. 7(a)[83].

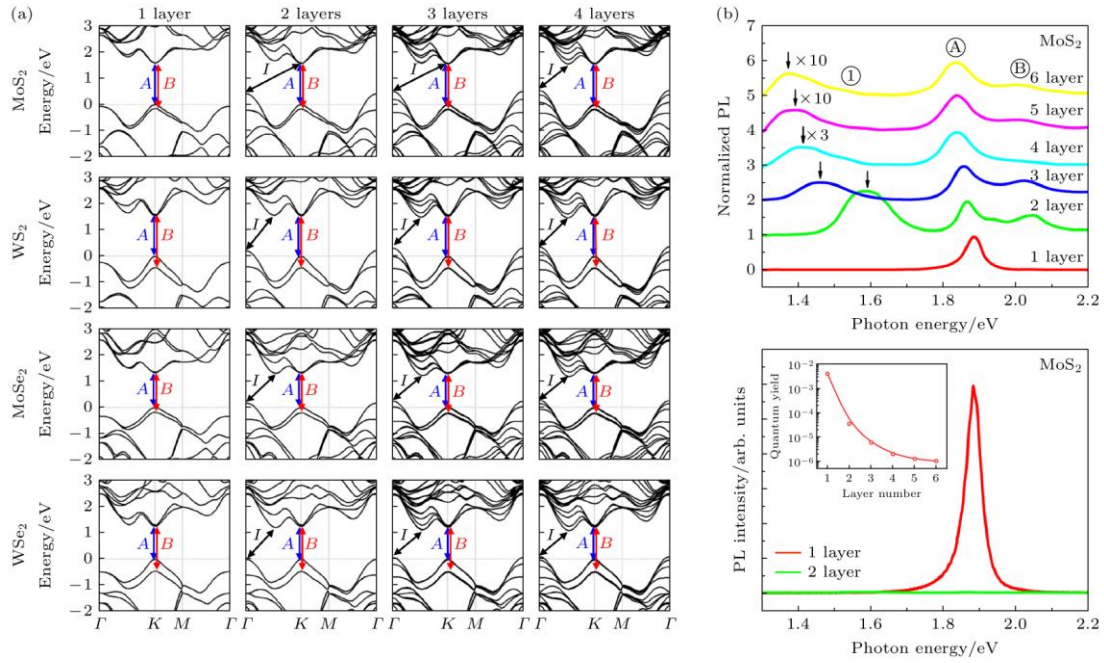

Figure 7. (a) Band structures of MoS_2, WS_2, $MoSe_2$, and WSe_2 with different thicknesses[84]; (b) (top) normalized PL spectra by the intensity of peak A of thin layers of MoS_2; (bottom) PL spectra for mono- and bilayer MoS_2 samples. Inset: PL quantum yield in different layer[19].

Different from the band gap of bulk TMD which decreases and closes under high pressure, the *K*-*K* band gap of monolayer TMD is believed to increase under high pressure[44,46,47,70,71,78,85,86]. It is worth noting that the *Λ*-*K* band gap decreases with the increase of pressure, resulting in the crossing of the *K* and the *Λ* at the CBM, which is the turning point from the blue shift to the red shift of the PL peak, taking MoS_2 as an example, as shown in Fig. 8(a)-(d). This occurs in MoS_2, WS_2, $MoSe_2$, and WSe_2 at about 1.9[44], 2.6[71], 3.7[86], and 2.3 GPa, respectively[85]. This behavior is considered to be mainly caused by the in-plane compression under pressure: the main contribution of the conduction band *K* point comes from the out-of-plane *d* orbital of the metal atom, while the *Λ* point is mainly the hybridization of the in-plane *d* orbital, which leads to the lattice compression and the change of the *X*-*M*-*X* bond angle, which has a greater impact on the *Λ* state and reduces its energy[44,82,87]. In addition to the high-pressure evolution of the PL peak position, double-resonance Raman (DDR) spectroscopy can also be used as a sensitive probe to detect the change of electronic structure. When the laser-excited electronic transition occurs between real states, the resonance results in a significant enhancement of the Raman signal intensity. In monolayer materials, the second-order resonance of the longitudinal phonon (LA) at the *M* point in the Brillouin zone, the 2LA (*M*) mode, is a specific mode associated with the conduction band *K*-*Λ* scattering, as shown in Fig. 8(e). The significant increase in intensity at high pressure is attributed to the decrease in the energy difference between the *K* and *Λ* valleys caused by the *K*-*Λ* crossing of the conduction band[87].

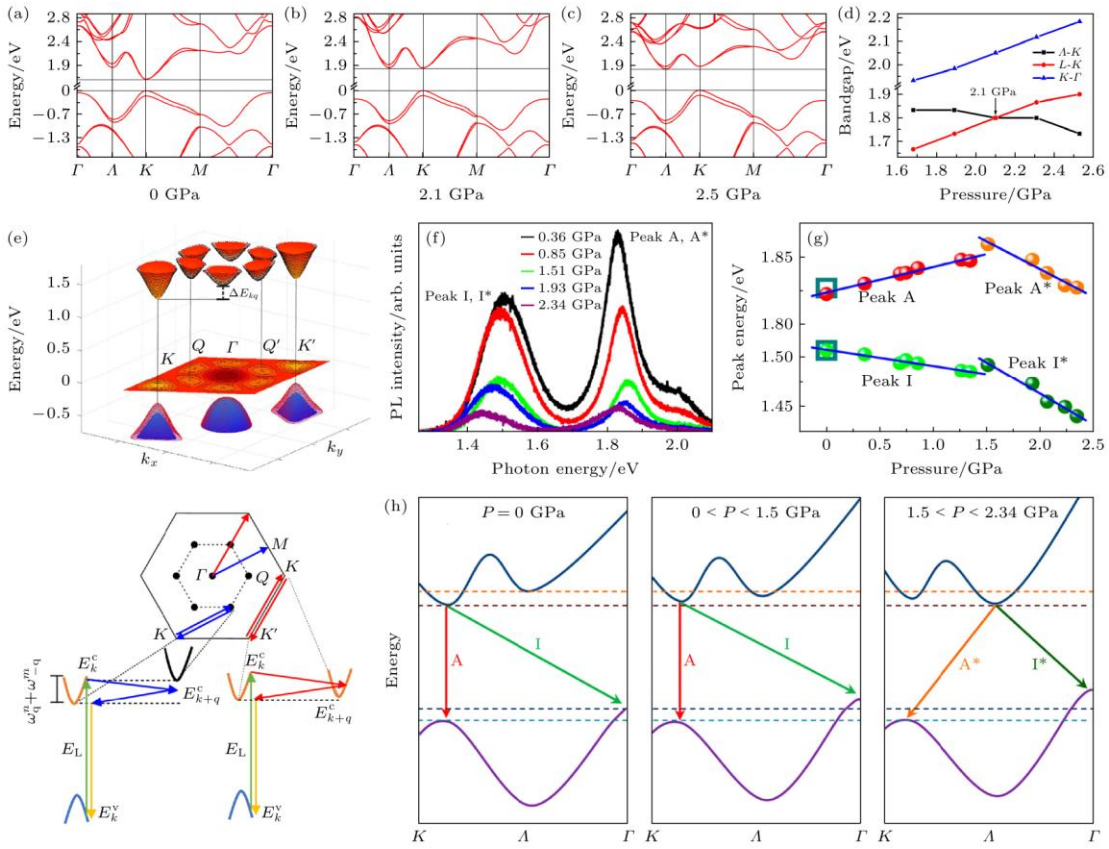

Figure 8. (a)–(c) Calculated band structures of monolayer MoS_2 at 0, 2.1, and 2.5 GPa, respectively[44]; (d) functional relationships of bandgap versus pressure on monolayer MoS_2[44]; (e) band structure of monolayer TMDs and schematic representation of the two-phonon DRR processes for monolayer MoS_2 and WSe_2 at ambient pressure, intervalley scattering between *K*-*Q*(*Λ*) as well as *K*-*K'* valleys can occur, the *K*-*Q* scattering is mostly mediated by phonons near *M*, while *K*-*K'* scattering involves phonons near *K*[87]; (f) PL spectra of the bilayer MoS_2 sample under high pressure[43]; (g) photon energies of the PL peaks of the bilayer MoS_2 as a function of pressure[43]; (h) schematic representations of the band structure for bilayer MoS_2 when P = 0 GPa, 0 GPa < P < 1.5 GPa, and 1.5 GPa < P < 2.34 GPa[43].

For bilayer and few-layer materials with interlayer interaction, it is generally believed that the band gap of *K*-*K* increases with pressure, which is consistent with the situation in monolayer, while the indirect band gap of *K*-*Γ* or *Λ*-*Γ* decreases with pressure, which is mainly due to the influence of enhanced interlayer interaction on band evolution under high pressure, and the principle is similar to the previous analysis on the layer number dependence of band structure at ambient pressure[43,70,71,85,88,89]. At the same time, for the bilayer MoS_2 with the CBM of *K*, the crossing of the conduction band bottom of *K*-*Λ* also occurs like the monolayer, as shown by Fig. 8(f)-(g)[43,70].

Although the band gap of both monolayer and few-layer eventually decreases under high pressure, metallization has not been observed experimentally, which is believed to be due to

the higher pressure required for band gap closing, such as the metallization pressure of monolayer MoS_2 predicted to be above 60 GPa[47]. In particular, unlike the metallized $2H_a$ MoS_2, the bilayer MoS_2 with interlayer sliding is considered to be unmetallized up to about 40 GPa[70].

As mentioned above, there is a large spin-orbit coupling splitting at the *K* point of the valence band (150-500 meV) and a small splitting at the *K* point of the conduction band (20-40 meV). In the absorption or emission spectrum, two peaks, peak A and peak B, corresponding to the *K*-*K* transition and due to the splitting of the valence band, are observed, and their energy difference corresponds to the size of the spin-orbit coupling splitting. The pressure control of the spin-orbit coupling splitting is mainly studied in MoS_2: the energy splitting is almost constant with pressure in monolayer MoS_2, while it increases with pressure in few-layer samples, and the energy difference in trilayer samples increases faster than that in bilayer samples[88–92]. In the monolayer, the energy splitting of the valence band is only related to its spin splitting ($2\lambda_V$) and is independent of the interlayer coupling strength *t*. In few-layer samples, the effect of interlayer coupling strength *t* should be considered, and the splitting is $2\sqrt{\lambda_V^2 + t^2}$. Under high pressure, the λ_V has no significant change, while the *t* increases significantly, and the coupling strength *t* of bilayer MoS_2 at 12.7 GPa (101 meV) is 2.8 times that at normal pressure (36 meV)[91]. The trilayer exhibits a larger energy splitting than the bilayer, due to its interlayer interactions being more susceptible to pressure. The increase of coupling strength *t* is due to the increase of atomic orbital wave function overlap caused by in-plane and out-of-plane lattice compression, of which the latter plays a major role, and the change of interlayer distance *d* leads to the change of *t* [91,92].

Under high pressure, the carrier mobility and concentration of few-layer or bulk semiconductor TMD will be significantly improved. In the electronic structure, the pressure-induced band gap decreases and the dispersion at the CBM increases, thus reducing the electron effective mass. Secondly, high pressure enhances the van der Waals interlayer interaction and promotes the interlayer carrier transport, which can help to improve the carrier mobility and concentration [93,94]. In particular, the enhancement effect of interlayer interaction is more significant in bulk materials, and the mobility enhancement is higher than that in few-layer samples [93].

3.3 Exciton

Exciton behavior in semiconductor TMD under high pressure is greatly influenced by its electronic structure, such as exciton energy. In addition, ultrafast spectroscopy provides a unique means to reveal the dynamic response mechanism of materials under high pressure, which helps to reveal the band evolution, exciton lifetime changes and carrier dynamics[95,96]. In monolayer $MoSe_2$, the exciton lifetime increases with pressure, as shown by the Fig.

9(a)-(b), which is believed to be due to the direct to indirect band gap transition discussed previously[97].

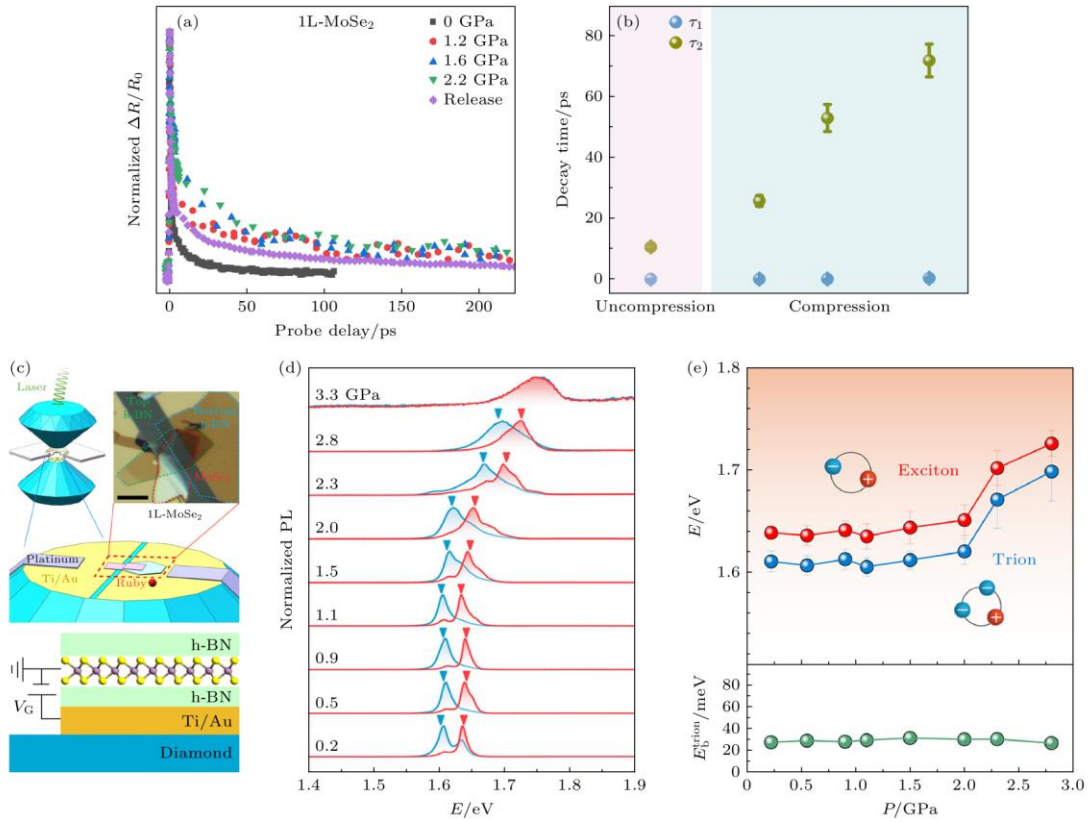

Figure 9. (a) Normalized differential reflection signals under high pressure in monolayer $MoSe_2$[97]; (b) the average values of fluorescence lifetime of two decay component τ_1 and τ_2 at different pump powers in monolayer $MoSe_2$ under uncompressed and compressed conditions[97]; (c) schematic illustration of the high-pressure gating *h*-BN/$MoSe_2$/*h*-BN heterostructure setup[98]; (d) normalized PL spectra of monolayer $MoSe_2$ under various pressures, the red (or blue) curve was obtained at V_G = –3 V (or 3 V)[98]; (e) pressure-dependent exciton and trion states of $MoSe_2$ obtained by PL measurements and E_b^{trion} as a function of pressure[98].

A trion is a charged excitonic complex composed of an exciton bound to either a free electron or a free hole, resulting in a negatively charged or a positively charged complex, respectively. In monolayer TMD, the trion binding energy E_b^{trion} (energy difference between trion and exciton) is 20-40 meV. In photoexcitation, a higher exciton density increases the possibility of forming exciton complexes, and negative trions are often seen in the PL spectra of monolayers[78,85,86]. In addition, electrons or holes can be injected into the material by applying an electrostatic field using a gate voltage. This increases the probability of forming the corresponding negative or positive trion, resulting in a relative enhancement of the trion signal in the PL spectra, which is beneficial for its detection and study. By combining a gate voltage with high pressure, the pressure evolution of the trion binding energy of monolayer

$MoSe_2$ is investigated as shown in the Fig. 9(c)[98]. It is worth noting that the binding energy is basically unchanged with pressure and remains at about 30 meV, as shown in Fig. 9(d)-(e). This is attributed to the cancellation of mass-dependent terms in the exciton and trion Hamiltonians, and the perturbative nature of the Hughes-Eckart term in the trion Hamiltonian, which leads to the relative stability of the trion binding energy as the electron and hole effective masses change under pressure[98]. From a simplified physical point of view, this can be understood by considering the trion as an electron bound to the exciton, which is spatially diffuse (a few nm in radius in $MoSe_2$) and overall charge neutral, so from an electronic point of view, the energy released by binding to the exciton can be considered constant[98].

3.4 Summary

In summary, the evolution of the layer-dependent crystal structure, electronic structure, and exciton properties under high pressure in the TMD are summarized. By comparing the behavior differences between monolayer and multilayer in various works, the effects of intralayer compression and interlayer interaction enhancement on the evolution of structural properties can be sorted out. In the aspect of structural evolution, the existence and enhancement of interlayer interaction increase the sensitivity of out-of-plane compression, but decrease the sensitivity of in-plane compression. The decrease of interlayer restoring force caused by the decrease of interlayer interaction is the key reason why the interlayer sliding phase transformation is more likely to occur at lower pressure. In particular, based on the Raman vibration and band splitting, the evolution of the interlayer interaction with the number of layers and pressure can be quantified, which lays the foundation for the proposal of various physical properties-interlayer interaction quantitative models[72,91]. It is worth noting that the MCM model is expected to predict the number of layers and high-pressure evolution behavior of the interlayer Raman modes of various two-dimensional materials [72]. For the electronic band, based on the electronic orbital hybridization characteristics of different valleys, the existence and enhancement of interlayer interaction contribute to the relative rise of the valence band Γ valley, the compression within the layer contributes to the increase of the *K*-*K* band gap, and both contribute to the relative decline of the conduction band Λ valley. Under high pressure, the weak interaction between layers is more significant than the intralayer compression, which dominates the high-pressure behavior of few-layer and bulk samples. In addition, in terms of exciton behavior, the unusual high-pressure robustness of the trion binding energy reveals many-body interactions in the TMD exciton state that go beyond the two-dimensional hydrogenic model.

4. TMD heterostructure or homostructure under high pressure.

4.1 Crystal structure evolution

As discussed above, by changing the number of layers of the TMD, the interaction between

the layers is regulated, which has an important impact on the behavior at ambient and high pressures. In addition to the number of layers, stacking can also affect the interaction between layers. Natural semiconductor TMD is mainly based on the 2*H* stacking. With the development of sample growth and transfer technology, homo- and heterostructures with different twist angles can be fabricated.

Unlike monolayers, homo- or heterostructures exhibit different behavior due to interlayer interactions, such as the Raman and PL spectral behavior discussed earlier [99–103]. At high pressure, as shown in Fig. 10(a), the out-of-plane vibrational mode A_1' (A_{1g}) in the heterostructure exhibit a significant frequency shift compared to those in the monolayer, whereas the in-plane E' (E_{2g}^1) mode does not exhibit such a shift, indicating that the interlayer coupling has little effect on the in-plane vibration, and the vertical vibration of the system is strongly renormalized[99,104,105]. In addition, similar to bilayer samples, structural phase transitions such as interlayer sliding or rotation also occur in homo- or heterostructures with pressure [106–109].

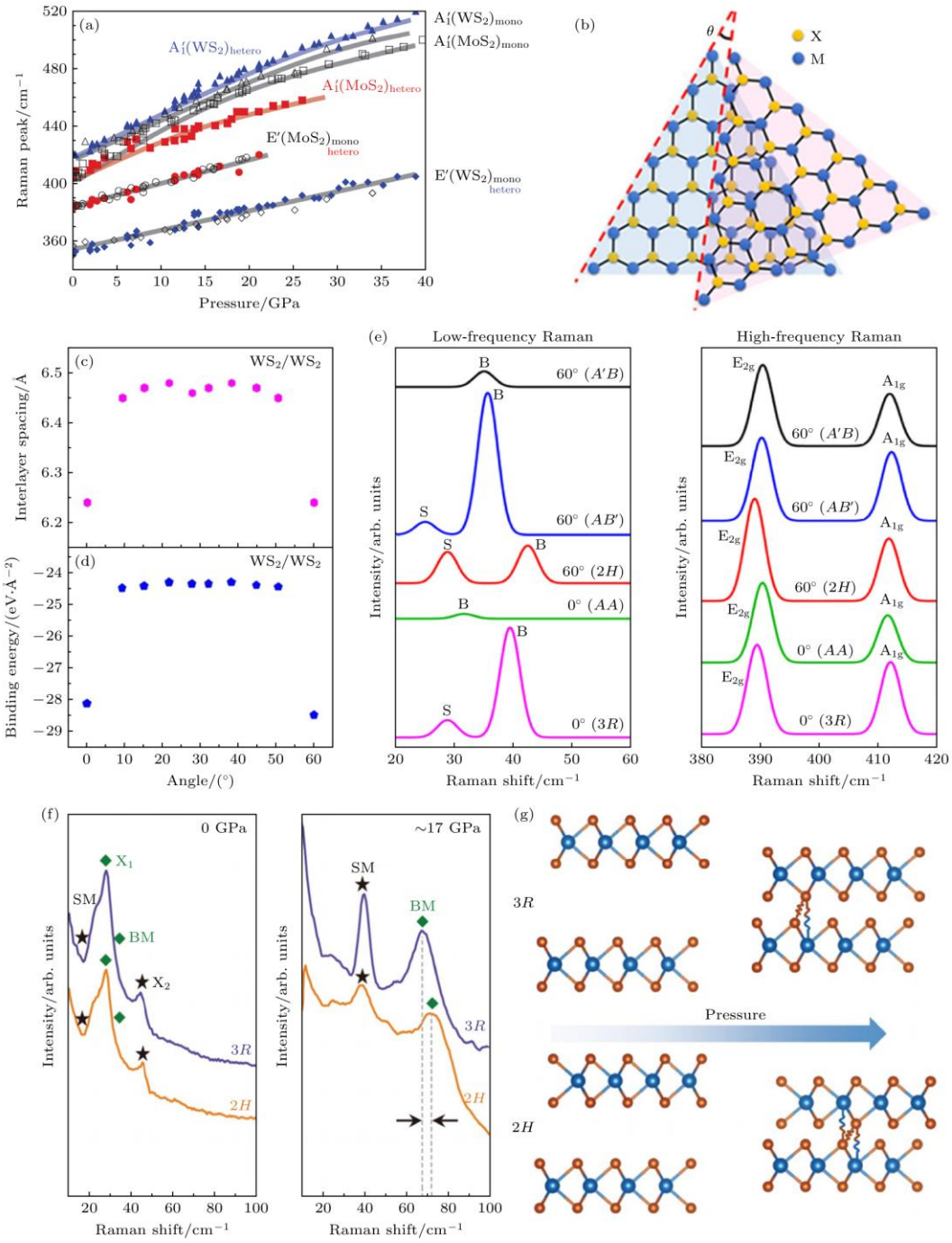

Figure 10. (a) Raman peak positions of the A_1' and E' vibration modes as a function of pressure on MoS_2/WS_2[104]; (b) schematic diagram of vertically stacked TMD with a twist angle of θ[100]; (c) the interlayer spacing, and (d) binding energy between two monolayers versus twist angles, as an example of WS_2[100]; (e) simulated Raman spectra of the five high-symmetry stackings at 0 ° and 60 °, as an example of twist bilayer MoS_2[102]; (f) Raman spectra in 3*R*- and 2*H*-stacked bilayer WS_2 under 0 and 17 GPa.[107]; (g) schematic of pressure induced interlayer compressing in 3*R*- and 2*H*-stacked bilayer WS_2[107].

In both homo- and heterostructures, the interlayer twist angle serves as a powerful tool for tuning interlayer interactions, as shown by Fig. 10(b)-(d). The modulation of the interlayer coupling originates from the change of the interlayer distance caused by the repulsion between two adjacent layers, as shown in Fig. 10(c)-(d), the interlayer coupling strength is generally the strongest in the twist angle of 0 ° or 60 °. When the twist angle is between 0 ° and 60 °, the interlayer coupling strength becomes weak and reaches a minimum at about 30 °[100–103]. 2*H* stacking corresponds to an interlayer twist angle of 60 °, 3*R* stacking corresponds to 0 °.

Heterostructures with different twist angles have different pressure responses under high pressure due to the difference of interlayer coupling, such as the evolution of Raman peak position and different phase transition paths[108,110]. It is worth noting that although both 3*R* and 2*H* stacking are the maximum points of interlayer coupling strength, they also have differences, which can be reflected in the low-frequency interlayer Raman mode, as shown in the Fig. 10(e)[102,111]. And the 2*H* and 3*R* stacked homostructures also show different pressure evolutions under high pressure[106,107]. In particular, bilayer 3*R*- and 2*H*-WS_2 exhibit small stacking dependence on Raman at ambient pressure due to the larger interlayer distance. Pressure can effectively adjust the interlayer coupling, and a significant stacking dependence is observed, that is, the frequency and pressure evolution rate of the interlayer Raman mode are different, as shown in Fig. 10(f)[107]. Specifically, as shown in Fig. 10(g), the next-nearest W-S interaction is doubled in the 2*H* stack compared to the 3*R* stack, resulting in a higher stiffness coefficient for the interlayer breathing mode and thus a higher Raman frequency[107].

4.2 Electronic structure evolution

The TMD heterostructure is generally type II heterostructure, that is, the CBM and the VBM are located in different materials, as shown by Fig. 11(a)[112]. In addition, the interlayer interaction leads to the increase of the valence band Γ point energy and the decrease of the conduction band Λ point energy relative to the monolayer. This band shift may even cause the heterostructure to exhibit an indirect band gap. For example, the energy of the valence band Γ point in MoS_2/WS_2 is higher than that of the *K* point, as shown by Fig. 11(b)-(c), which is similar to that of natural bilayer materials. As discussed earlier, the evolution of the interlayer interaction due to twist angle also regulates the electronic structure, such as the size of the band gap. Generally, the band gap is the smallest near 0 ° or 60 °, and the band gap is the largest near 30 °, as shown in Fig. 11(d)-(e) using $MoSe_2/WS_2$[113,114] as an example.

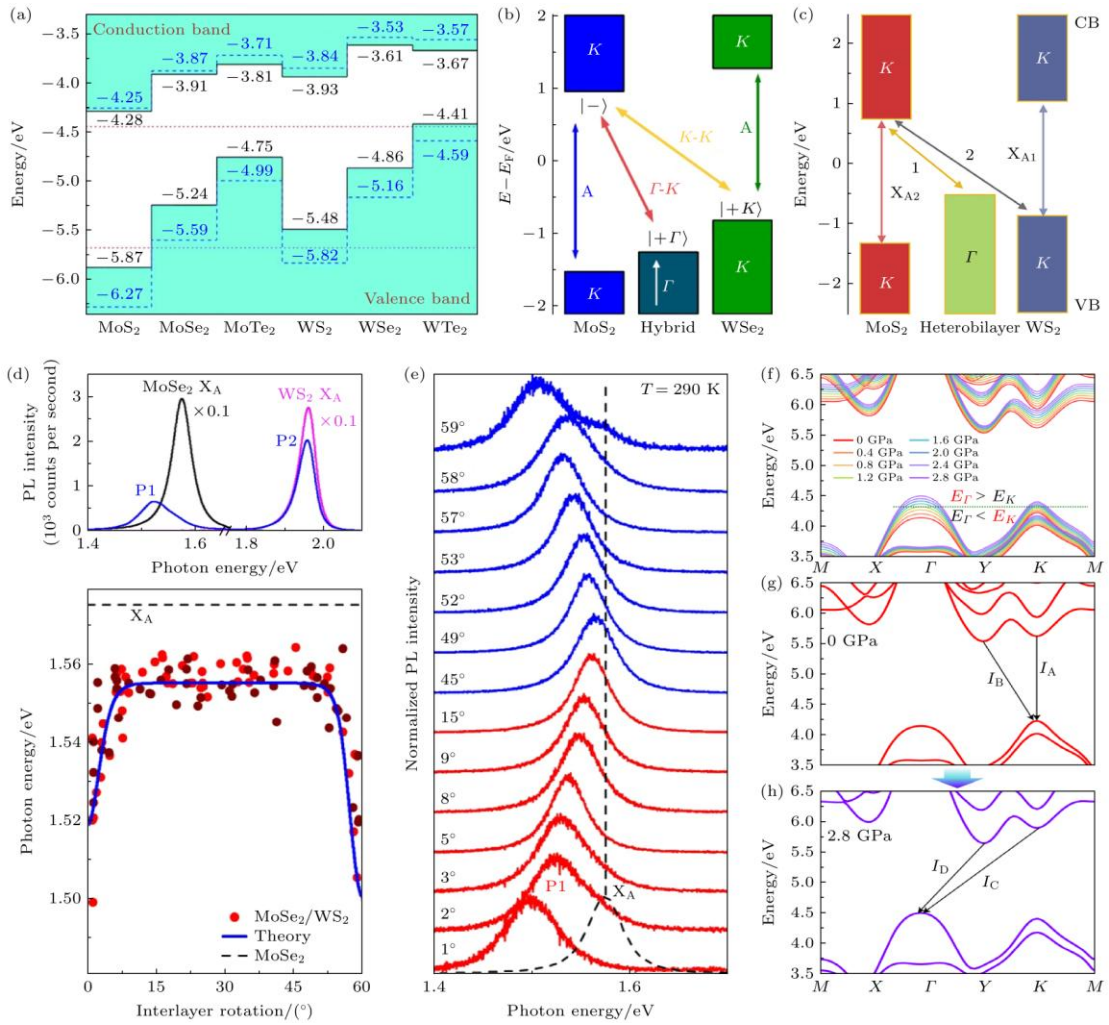

Figure 11. Band alignment for (a) MX_2 monolayers[112], (b) MoS_2/WSe_2[115] and (c) MoS_2/WS_2 heterostructures[113]; (d) (top) PL spectra measured in $MoSe_2$ (black), WS_2 (pink) monolayers and $MoSe_2/WS_2$ heterostructure with a twist angle of 2 ° between the layers (blue); (bottom) Variation of the PL peak energy with twist angle in $MoSe_2/WS_2$; (e) normalized PL spectra in $MoSe_2/WS_2$ with interlayer twist angles ranging from 1 ° to 59 °[114]; (f)–(h) first-principles calculation results of electronic band structure of 2*H*-$WSe_2/MoSe_2$ heterostructures as a function of pressure in the 0–2.8 GPa range.[111]

Under high pressure, the MoS_2/WS_2 heterostructure undergoes a CBM crossover from the *K* to *Λ* valley at pressures between 1.22 and 1.89 GPa, which is similar to that of the monolayer discussed previously, while the transition pressure is lower than that of the monolayer due to the effect of interlayer interaction on the band structure[116]. WSe_2/WS_2 and 2*H*-$WSe_2/MoSe_2$ heterostructures undergo a VBM *K*-*Γ* crossover phase transition at about 4.0 and 1.0 GPa, respectively, as shown in Fig. 11(f)-(h)[111,117]. Interestingly, the band gap of the $WS_2/MoSe_2$ heterostructure shows only a weak pressure dependence, which is different from the obvious blue shift of the exciton energy in the monolayer materials [118]. This may be due to that the conduction band edge of WS_2 and the valence band edge of $MoSe_2$ move in the same

direction at a comparable rate [118].

4.3 Exciton

As mentioned above, in the TMD heterostructure of type II heterostructure, electrons and holes accumulate in the bottom of the conduction band and the top of the valence band of different layers, respectively, and the strong electron-hole Coulomb interaction between adjacent layers will produce spatially separated electron-hole pairs, called interlayer excitons. Due to this spatially indirect nature, the overlap of the electron and hole wave functions in the interlayer exciton is reduced, which significantly increases the exciton lifetime to hundreds of nanoseconds, much higher than the picosecond level in monolayer samples[119,120]. Long-lived interlayer excitons contribute to new optoelectronic applications such as solar cells and photodetectors, especially the development of potential excitonic circuits with remote exciton transport properties [121–125]. At the same time, based on its bosonic nature and strong dipole-dipole interaction, it has established an attractive platform for exploring many-body physical phenomena such as Bose-Einstein condensation and exciton superfluidity.

The enhanced interlayer coupling by compressing the interlayer distance under pressure can promote the combination of electrons and holes in different layers and increase the formation probability of interlayer excitons, as shown in Fig. 12(a). Experimentally, in the $WS_2/MoSe_2$ heterostructure, the intralayer exciton peak disappears after 3.8 GPa, while the interlayer exciton persists up to 8.9 GPa, as shown by Fig. 12(b)-(c), which verifies that the interlayer coupling enhances the transition from the intralayer exciton to the interlayer exciton[118]. However, it is the accelerated recombination of spatially separated electrons and holes under pressure that significantly shortens the lifetime of the interlayer exciton by an order of magnitude at about 2 GPa[97].

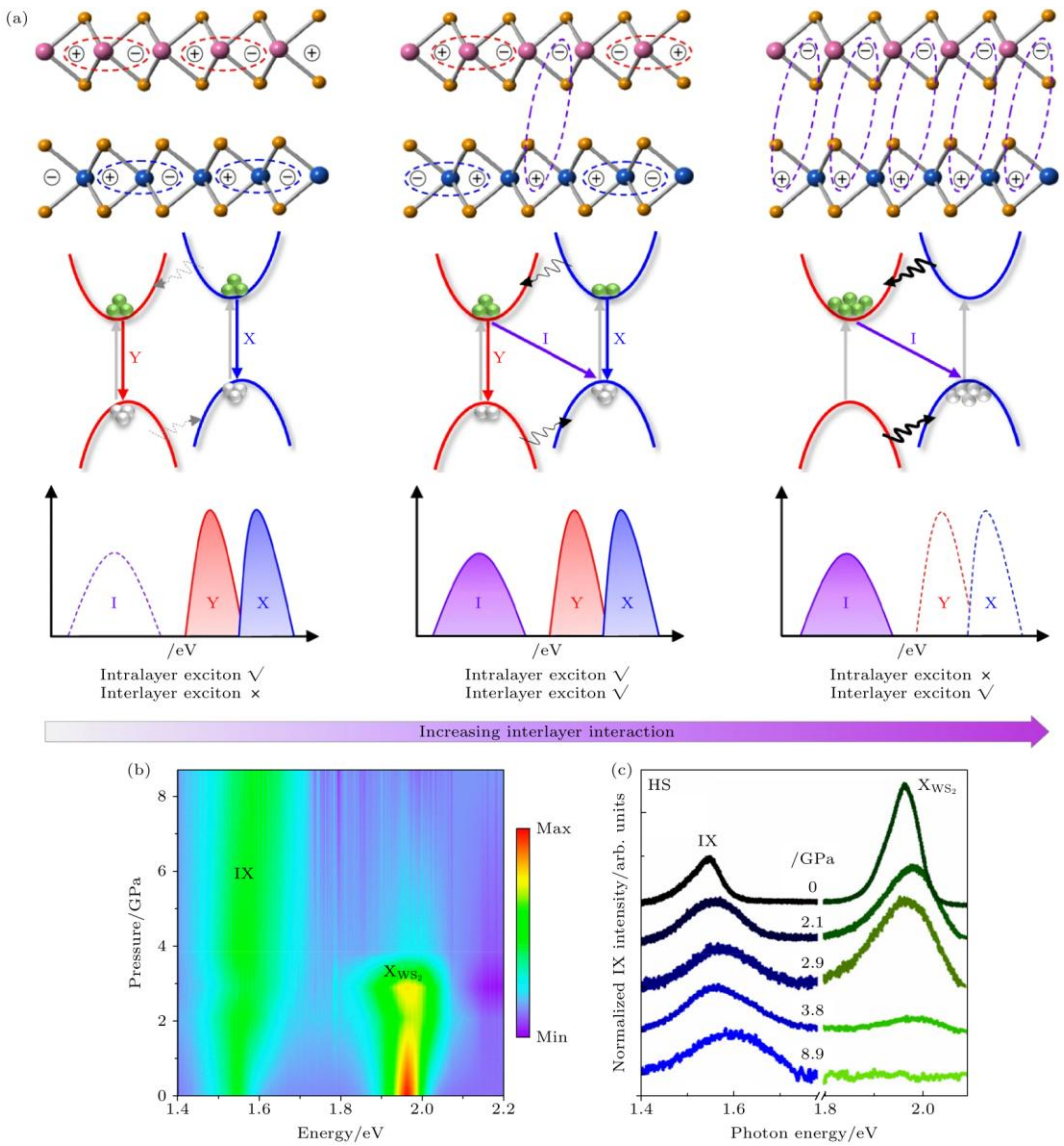

Figure 12. (a) Evolution of the behavior of exciton in type-Ⅱ-alignment 2D heterostructures with increasing interlayer interaction strengths[111]; (b), (c) normalized PL spectra on $WS_2/MoSe_2$ heterostructure under different pressures[118].

4.4 Moiré potential

Notably, Moiré superlattice appears in TMD homo- and heterostructures, where lattice mismatch or twist angle leads to the formation of large periodic structures, Moiré patterns, as shown by Fig. 13(a). In TMD, the Moiré superlattice varies from a few nanometers to tens of nanometers based on different lattice mismatches and twist angles. The coupling strength of the electronic states of the two layers at different stacking sites is different, which leads to spatial modulations in both the local interlayer distance and the band gap. This modulation forms a periodic potential well, moiré periodic potential, with a depth of 100-250 meV, and the well extrema are located at the high symmetry positions of the moiré superlattice, as shown by Fig. 13(a)-(b)[39,126–129]. The Moiré potential can be used to trap intralayer or

interlayer excitons and modulate their energy and optical properties. The trapped Moiré excitons can be used as single photon emitters and quantum simulation systems [130,131]. More notably, the Moiré superlattice forms a mini Brillouin zone (mBZ) through the folding of energy bands, and the opening of the band gap at the mBZ boundary forms a flat band, as shown by Fig. 13(c)-(d). The strong interaction regime associated with flat bands establishes a platform for emergent strongly correlated phenomena in two-dimensional systems, such as unconventional superconductivity, ferromagnetism, and correlated insulating phases. Therefore, TMD heterostructure provides a new and more controllable platform for the study of strong correlation physics and quantum simulation.

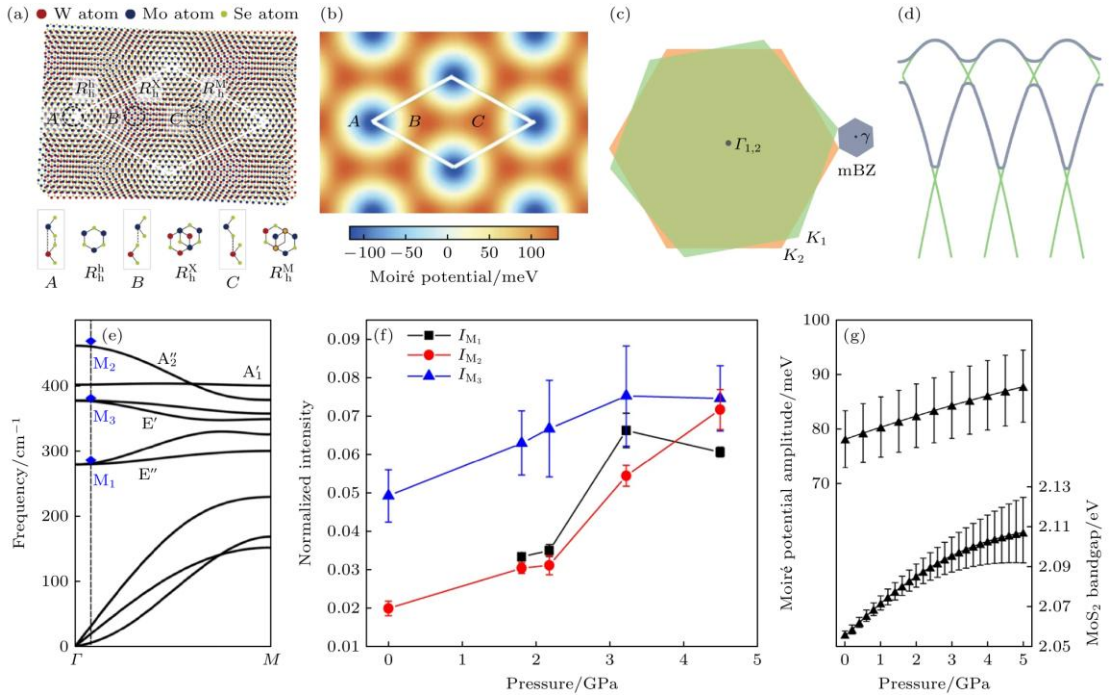

Figure 13. (a) (Top) Moiré pattern in an *R*-type $MoSe_2/WSe_2$ heterostructure, (bottom) side-views and top-views of the three *R*-type local atomic registries (*A*, *B*, and *C* sites)[129]; (b) the moiré potential of the interlayer exciton transition in an *R*-type $MoSe_2/WSe_2$ heterostructure[129]; (c) schematic of the Brillouin zones of each monolayer (green and orange) and the mBZ of the superlattice[29]; (d) schematic of monolayer bands (green) folded in the mBZ, the moiré potential opens a gap at the mBZ boundary, which produces flatter electronic bands (grey)[29]; (e) DFT-calculated phonon dispersion of MoS_2 at ambient pressure along the *Γ*-*M* direction, the vertical dashed line indicates the moiré vector. The blue symbols represent the moiré phonon M1-, M2- and M3-peak frequencies obtained from the Raman spectra at ambient pressure[132]; (f) pressure evolution of the normalized intensities of moiré phonons[132]; (g) calculated moiré potential amplitude and MoS_2 bandgap in the heterostructure as functions of pressure[132].

In the moiré superlattice, the moiré potential depth at the $\boldsymbol{r}$ position is $V_{\mathrm{M}}(r) = V_0 + V_1 \sum_{n=1}^{3} \sin(g_n \cdot r)$, where the constant term V_0 of the moiré potential is of the order of 10 meV, g_n are reciprocal lattice vectors of the moiré pattern (n = 1, 2, 3), and V_1 is a Moiré potential parameter that increases exponentially with decreasing interlayer distance d and is related to pressure by: $V_1(P) = V_1(0) \times \mathrm{e}^{-q_z(d(P)-d(0))}$ [132,133]. Under high pressure, the interlayer spacing d in van der Waals heterostructure is significantly reduced by compression, resulting in a significant increase in the depth of the Moiré potential. It is worth noting that the Moiré periodic potential can modulate phonon as well as exciton behavior. Therefore, by observing the evolution of phonon and exciton behavior in the Moiré potential under high pressure, we can reveal the change of Moiré potential caused by high pressure, especially verify the significant increase of its potential well.

The effect of Moiré potential enhancement on phonons under high pressure is discussed first. The introduction of the Moiré superlattice generates Moiré phonons, which originate from the Raman silent phonons of finite momentum generated in each layer and are activated due to the folding of the phonon bands in the mBZ, so that they can be detected by Raman spectroscopy. The folded phonons can couple with the low frequency breathing mode in small twist angle 2 ° and 5 °-WSe_2/WSe_2 homostructures[105]. Under high pressure, the blue shift rate of the low frequency breathing mode in the Moiré homostructure is 2-3 times that of the natural 2H bilayer, and a larger twist angle corresponds to a larger blue shift rate [105]. The mechanism is due to the deepening of the Moiré potential at high pressure, which enhances the coupling between the folded phonon and the interlayer breathing mode.

It is worth noting that when the depth of the Moiré potential increases, the Hamiltonian of the electron-photon interaction in Raman scattering increases, which increases the Raman amplitude of the Moiré phonon[132]. Therefore, moiré phonons provide a powerful means of directly probing the depth of the moiré potential. Moiré phonons M1, M2, M3, which are generated by phonon band folding of MoS_2, are observed in 0 °-MoS_2/WSe_2 heterostructure, and their intensities increase with pressure, as shown by Fig. 13(e)-(f)[132]. A numerical estimate of the pressure dependence of the moiré potential depth V_{M} is obtained by comparing the experimental and calculated Raman intensity enhancement, as shown in Fig. 13(g). In addition, in the 30 °-MoS_2/MoS_2 homojunction, the phonon mode FA_{1g} formed by the band folding of A_{1g} mode is observed experimentally, and its blue shift rate under high pressure is significantly higher than that of A_{1g} mode. Theoretical calculations reveal that the high rate of the blue shift for the dominant folded phonon mode originates from the compression of the interlayer distance [134]. Therefore, the shift of the folded phonon frequency relative to the original phonon frequency at high pressure is also expected to be a sensitive probe for detecting the pressure enhancement effect of the Moiré potential. Finally, it is generally believed that the distance between layers at high pressure decreases nonlinearly with the

increase of pressure, and the rate of decrease decreases with the increase of pressure, while the depth of Moiré potential increases nearly linearly with the pressure[132,134].

The potential well of the Moiré periodic potential may trap the exciton, and the energy of the exciton trapped in the potential well will be reduced. The depth of the Moiré potential can be directly revealed by the energy difference between trapped and untrapped excitons. Under high pressure, the deepening of the Moiré potential will transfer the trapped exciton to a lower energy, resulting in a red shift of the exciton emission peak [110,135]. Experimentally, by comparing the blue shift of the interlayer exciton in the WS_2/WSe_2 heterostructure with a large twist angle (7.5 °), the increase of the band gap obtained by band calculation, and the red shift of the interlayer exciton in the WS_2/WSe_2 heterostructure with a small twist angle (1.15 °) under high pressure, it is concluded that the exciton red shift in the small twist angle is mainly attributed to the deepening of the Moiré potential well caused by pressure, rather than the change of the band structure. In the large twist angle, the exciton energy is mainly affected by the increase of the band gap due to the shallow Moiré potential [110].

4.5 Summary

To sum up, the high-pressure evolution of crystal and electronic structure in heterostructure is similar to that in monomer, and is dominated by interlayer interaction. In particular, the interlayer twist angle introduced in the heterostructure becomes another dimension to regulate the interlayer interaction, which can change the interlayer hybridization of orbitals by changing the relative position of atoms, thus making up for the limitation of high pressure to regulate the symmetry of atomic positions. Under the compression of the interlayer distance, the interlayer exciton is easier to form and annihilate due to the enhancement of the wave function overlap. The deepening effect of Moiré potential under high pressure is quantitatively predicted by the evolution of Moiré phonon and exciton behavior. The enhanced interlayer exciton effect and Moiré potential will lead to the emergence of novel exciton states and related states in Moiré superlattices under high pressure control, and break through the low temperature limit.

5. Summary and Prospect

Returning to the four key scientific questions posed in Section1, we now summarize the current progress from these four directions, and predict the direction of future research work according to the limits of existing research.

1) High pressure evolution of crystal structure and electronic structure. At present, the high-pressure evolution and phase transition mechanism of the crystal structure and electronic band structure of monomer and heterostructure are relatively clear. The transport properties under high pressure, such as carrier concentration, carrier mobility and superconductivity, have also been revealed. However, some important problems remain to be solved, especially

the metallization and superconductivity of monolayer and few-layer materials under high pressure. It is worth noting that the superconductivity in monolayer and few-layer TMDs is controlled by gate voltage doping at ambient pressure, and shows quantum properties such as two-dimensional superconductivity and unconventional Ising superconductivity[136–140]. In future studies, potential superconductivity may be revealed through ultrahigh-pressure experiments, potentially revealing distinct superconducting mechanisms compared with different electronic band structures at ambient pressure. In addition, through the combined regulation of pressure and gating, the high-pressure-induced *K* to *Λ* valley crossing may enhance the superconducting properties of few-layer TMD based on *K* to *Λ* intervalley scattering, and help to further clarify the role of intervalley scattering in the superconducting mechanism[139,140].

2) Interlayer interaction. In the high-pressure study of TMD, the key role of interlayer interaction and its specific mechanism have been revealed, especially the high pressure can achieve a wide range of continuous quantitative regulation of interlayer interaction. Future research can be devoted to extending the laws summarized in TMD, such as MCM and DCM models, to other two-dimensional materials, exploring their similarities and differences, and finally establishing a universal quantitative model to describe the evolution of interlayer interaction with the number of layers and pressure, and to clarify the mechanism of its regulation of physical properties.

3) Exciton complexes. At present, only the high-pressure robustness of the trion binding energy of monolayer $MoSe_2$ has been revealed under high pressure. For other materials, such as W-based monolayer TMD with different spin ground state, it is not clear whether the trion exhibits different characteristics. In addition, there is a lack of research on other properties of trions and the high-pressure behavior of many other types of exciton complexes. The properties and formation mechanism of exciton complexes have attracted much attention. Future research can combine high pressure, low temperature, magnetic field and gate voltage for multi-field control. To engineer more controllable exciton states and to uncover new emergent phases, research efforts are concentrated on phenomena such as enhanced valley polarization and prolonged lifetimes. These effects are driven by the high-pressure-enhanced electronic state overlap and concomitant band structure modifications. These studies have great potential in the fields of valley optoelectronics devices and quantum information processing. In addition, the many-body interaction mechanism between excitons and various particles and quasiparticles in excitonic complexes is revealed by the evolution of the binding energy, polarizability, valley magnetic moment, lifetime and other properties of various exciton complexes under high pressure.

4) Moiré potential. At present, the deepening of Moiré potential depth under high pressure is focused on, and the evolution relationship is quantitatively predicted. First, the specific

quantitative dependence of the Moiré potential depth on pressure requires a more direct experimental determination. For example, an atomically thin layer of hBN can be inserted in the middle of a Moiré heterostructure to separate regions with and without Moiré potential. By directly comparing the exciton energy difference between the two regions, the Moiré potential depth can be directly obtained. Secondly, the related states in Moiré superlattices, such as Mott insulator, Wigner crystal, exciton superfluid state, etc., have been obtained by gate voltage control at ambient pressure and have attracted much attention, but their evolution at high pressure is still lacking[9,34,36,141–146]. By fabricating devices in a high-pressure cavity, the study of the evolution behavior of correlated states in a deep Moiré potential, especially the emergence of novel correlated states and their temperature stability that may be improved by high pressure, will help to further reveal the formation mechanism of correlated states. In particular, through the piston-cylinder cell mentioned above, the complex exciton transport devices on silicon wafers at ambient pressure can be more easily used for high-pressure measurement [146]. Finally, it is worth noting that the change of lattice constant or valley switching caused by high pressure may lead to the change of Moiré superlattice symmetry. For example, theoretical calculations show that the transition from the *K* valley to the *Γ* valley at the CBM in the twist WSe_2 bilayer can realize the switching from the triangular Moiré lattice to the honeycomb lattice Hubbard model[147–150]. Through the evolution of exciton optical selection rules and related states in Moiré superlattice under high pressure, the possible change of Moiré superlattice is explored, which is expected to reveal more abundant physical phenomena in Moiré potentials with different symmetries.

References

[1] Novoselov K S, Geim A K, Morozov S V, Jiang D, Zhang Y, Dubonos S V, Grigorieva I V, Firsov A A 2004 Science 306 666

[2] Chen H, Müller M B, Gilmore K J, Wallace G G, Li D 2008 Adv. Mater. 20 3557

[3] Geim A K, Novoselov K S 2007 Nat. Mater. 6 183

[4] Bolotin K I, Sikes K J, Jiang Z, Klima M, Fudenberg G, Hone J, Kim P, Stormer H L 2008 Solid State Commun. 146 351

[5] Chen K, Zhou X, Cheng X, Qiao R X, Cheng Y, Liu C, Xie Y D, Yu W T, Yao F R, Sun Z P, Wang F, Liu K H, Liu Z F 2019 Nat. Photonics 13 754

[6] Lee C, Wei X, Kysar J W, Hone J 2008 Science 321 385

[7] Lee C, Li Q, Kalb W, Liu X Z, Berger H, Carpick R W, Hone J 2010 Science 328 76

[8] Cao Y, Fatemi V, Fang S, Watanabe K, Taniguchi T, Kaxiras E, Jarillo-Herrero P 2018 Nature 556 43

[9] Cao Y, Fatemi V, Demir A, Fang S, Tomarken S L, Luo J Y, Sanchez-Yamagishi J D, Watanabe K, Taniguchi T, Kaxiras E, Ashoori R C, Jarillo-Herrero P 2018 Nature 556 80

[10]Hanlon D, Backes C, Doherty E, Cucinotta C S, Berner N C, Boland C, Lee K, Harvey A, Lynch P, Gholamvand Z, Zhang S, Wang K, Moynihan G, Pokle A, Ramasse Q M, McEvoy N, Blau W J, Wang J, Abellan G, Hauke F, Hirsch A, Sanvito S, O'Regan D D, Duesberg G S, Nicolosi V, Coleman J N 2015 Nat. Commun. 6 8563

[11] Qiao J S, Kong X H, Hu Z X, Yang F, Ji W 2014 Nat. Commun. 5 4475

[12] Lebedev A V, Blatter G 2011 Phys. Rev. Lett. 107 076803

[13] Qian X F, Liu J W, Fu L, Li J 2014 Science 346 1344

[14] Vogt P, De Padova P, Quaresima C, Avila J, Frantzeskakis E, Asensio M C, Resta A, Ealet B, Le Lay G 2012 Phys. Rev. Lett. 108 155501

[15] Tian Y J, Xu B, Yu D L, Ma Y M, Wang Y B, Jiang Y B, Hu W T, Tang C C, Gao Y F, Luo K, Zhao Z S, Wang L M, Wen B, He J L, Liu Z Y 2013 Nature 493 385

[16] Liu X B, Chen X, Ma H A, Jia X P, Wu J S, Yu T, Wang Y B, Guo J G, Petitgirard S, Bina C R, Jacobsen S D 2016 Sci. Rep. 6 30518

[17] Watanabe K, Taniguchi T, Kanda H 2004 Nat. Mater. 3 404

[18] Kubota Y, Watanabe K, Tsuda O, Taniguchi T 2007 Science 317 932

[19] Mak K F, Lee C, Hone J, Shan J, Heinz T F 2010 Phys. Rev. Lett. 105 136805

[20] Cao T, Wang G, Han W P, Ye H Q, Zhu C R, Shi J R, Niu Q, Tan P H, Wang E G, Liu B L, Feng J 2012 Nat. Commun. 3 887

[21] Wang Q H, Kalantar-Zadeh K, Kis A, Coleman J N, Strano M S 2012 Nat. Nanotechnol. 7 699

[22] Xiao D, Liu G B, Feng W, Xu X, Yao W 2012 Phys. Rev. Lett. 108 196802

[23] Song I, Park C, Choi H C 2015 RSC Adv. 5 7495

[24] Manzeli S, Ovchinnikov D, Pasquier D, Yazyev O V, Kis A 2017 Nat. Rev. Mater. 2 17033

[25] He K L, Poole C, Mak K F, Shan J 2013 Nano Lett. 13 2931

[26] Xu M S, Liang T, Shi M M, Chen H Z 2013 Chem. Rev. 113 3766

[27] Geim A K, Grigorieva I V 2013 Nature 499 419

[28] Chen X T, Lian Z, Meng Y Z, Ma L, Shi S F 2023 Nat. Commun. 14 8233

[29] Regan E C, Wang D, Paik E Y, Zeng Y, Zhang L, Zhu J, MacDonald A H, Deng H, Wang F 2022 Nat. Rev. Mater. 7 778

[30] Du L 2024 Nat. Rev. Phys. 6 157

[31] Wilson N P, Yao W, Shan J, Xu X 2021 Nature 599 383

[32] Jin C, Regan E C, Yan A, Iqbal Bakti Utama M, Wang D, Zhao S, Qin Y, Yang S, Zheng Z, Shi S, Watanabe K, Taniguchi T, Tongay S, Zettl A, Wang F 2019 Nature 567 76

[33] Seyler K L, Rivera P, Yu H, Wilson N P, Ray E L, Mandrus D G, Yan J, Yao W, Xu X 2019 Nature 567 66

[34] Regan E C, Wang D, Jin C, Bakti Utama M I, Gao B, Wei X, Zhao S, Zhao W, Zhang Z, Yumigeta K, Blei M, Carlström J D, Watanabe K, Taniguchi T, Tongay S, Crommie M, Zettl A, Wang F 2020 Nature 579 359

[35] Tang Y H, Li L Z, Li T X, Xu Y, Liu S, Barmak K, Watanabe K, Taniguchi T, MacDonald A H, Shan J, Mak K F 2020 Nature 579 353

[36] Xu Y, Liu S, Rhodes D A, Watanabe K, Taniguchi T, Hone J, Elser V, Mak K F, Shan J 2020 Nature 587 214

[37] Guo Y, Pack J, Swann J, Holtzman L, Cothrine M, Watanabe K, Taniguchi T, Mandrus D G, Barmak K, Hone J, Millis A J, Pasupathy A, Dean C R 2025 Nature 637 839

[38] Liu Z 2024 Acta Phys. Sin. 73 207303

[39] Tang Y H 2023 Acta Phys. Sin. 72 027802

[40] Pei S H, Wang Z H, Xia J 2022 Mater. Des. 213 110363

[41] Cheng X R, Li Y Y, Shang J M, Hu C S, Ren Y F, Liu M, Qi Z M 2018 Nano Res. 11 855

[42] Chi Z H, Zhao X M, Zhang H, Goncharov A F, Lobanov S S, Kagayama T, Sakata M, Chen X J 2014 Phys. Rev. Lett. 113 036802

[43] Dou X M, Ding K, Jiang D S, Sun B Q 2014 ACS Nano 8 7458

[44] Fu L, Wan Y, Tang N, Ding Y M, Gao J, Yu J C, Guan H M, Zhang K, Wang W Y, Zhang C F, Shi J J, Wu X, Shi S F, Ge W K, Dai L, Shen B 2017 Sci. Adv. 3 e1700162

[45] Hromadová L, Martoňák R, Tosatti E 2013 Phys. Rev. B 87 144105

[46] Li F F, Yan Y L, Han B, Li L, Huang X L, Yao M G, Gong Y B, Jin X L, Liu B L, Zhu C R, Zhou Q, Cui T 2015 Nanoscale 7 9075

[47] Nayak A P, Pandey T, Voiry D, Liu J, Moran S T, Sharma A, Tan C, Chen C H, Li L J,

Chhowalla M, Lin J F, Singh A K, Akinwande D 2015 Nano Lett. 15 346

[48] Okajima M, Endo S, Akahama Y, Narita S I 1984 Jpn. J. Appl. Phys. 23 15

[49] Li Q, Wang Y G, Pan W C, Yang W, Zou B, Tang J, Quan Z W 2017 Angew. Chem. , Int. Ed. 56 15969

[50] Errandonea D, Bandiello E, Segura A, Hamlin J J, Maple M B, Rodriguez-Hernandez P, Muñoz A 2014 J. Alloys Compd. 587 14

[51] Zhou Y H, Chen X L, Li N, Zhang R R, Wang X, F An C, Zhou Y, Pan X C, Song F Q, Wang B G, Yang W G, Yang Z R, Zhang Y H 2016 AIP Adv. 6 075008

[52] Vellinga M B, de Jonge R, Haas C 1970 J. Solid State Chem. 2 299

[53] XU J A, Mao H G, Bell L P 1987 Acta Phys. Sin. 36 501

[54] Ana B G, Gábor M, Aurelian R, Helena J S 2018 C. R. Chim. 21 1095

[55] Akahama Y, Kawamura H 2006 J. Appl. Phys. 100 043516 DOI:

[56] Li T, Jiang S, Sivadas N, Wang Z, Xu Y, Weber D, Goldberger J E, Watanabe K, Taniguchi T, Fennie C J, Fai Mak K, Shan J 2019 Nat. Mater. 18 1303

[57] Yankowitz M, Jung J, Laksono E, Leconte N, Chittari B L, Watanabe K, Taniguchi T, Adam S, Graf D, Dean C R 2018 Nature 557 404

[58] Yao X D, Bai Y X, Jin C, Zhang X Y, Zheng Q F, Xu Z D, Chen L, Wang S M, Liu Y, Wang J L, Zhu J L 2023 Nat. Commun. 14 4301

[59] Shen G, Wang Y, Dewaele A, Wu C, Fratanduono D E, Eggert J, Klotz S, Dziubek K F, Loubeyre P, Fat'yanov O V, Asimow P D, Mashimo T, Wentzcovitch R M M 2020 High Pressure Res. 40 299

[60] Yamaoka H, Zekko Y, Jarrige I, Lin J F, Hiraoka N, Ishii H, Tsuei K D, Mizuki J i 2012 J. Appl. Phys. 112 124503 DOI:

[61] Noack R A, Holzapfel W B (Timmerhaus K D, Barber M S ed) 1979 High-Pressure Science and Technology: Volume 1: Physical Properties and Material Synthesis/Volume 2: Applications and Mechanical Properties (Boston, MA: Springer US) pp748–753

[62] Yen J, Nicol M 1992 J. Appl. Phys. 72 5535

[63] Tardieu A, Cansell F, Petitet J P 1990 J. Appl. Phys. 68 3243

[64] Wang X F, Chen X L, Zhou Y H, Park C Y, An C, Zhou Y, Zhang R R, Gu C C, Yang W, Yang Z R 2017 Sci. Rep. 7 46694

[65] Duwal S, Yoo C S 2016 J. Phys. Chem. C 120 5101

[66] Zhao Z, Zhang H J, Yuan H T, Wang S B, Lin Y, Zeng Q S, Xu G, Liu Z X, Solanki G K, Patel K D, Cui Y, Hwang H Y, Mao W L 2015 Nat. Commun. 6 7312

[67] Lee C, Yan H, Brus L E, Heinz T F, Hone J, Ryu S 2010 ACS Nano 4 2695

[68] Zhao W, Ghorannevis Z, Amara K K, Pang J R, Toh M, Zhang X, Kloc C, Tan P H, Eda G 2013 Nanoscale 5 9677

[69] Molina-Sánchez A, Wirtz L 2011 Phys. Rev. B 84 155413

[70]Li C K, Liu Y Y, Yang Q S, Zheng Q F, Yan Z P, Han J, Lin J H, Wang S M, Qi J B, Liu Y, Zhu J L 2022 J. Phys. Chem. Lett. 13 161

[71] Luo J H, Li C K, Liu J Y, Liu Y Y, Xiao W H, Zheng R H, Zheng Q F, Han J, Zou T, Cheng W J, Yao X D, Liu Y, Zhu J L 2024 Appl. Phys. Lett. 124 033104

[72] Du G S, Zhao L L, Li S C, Huang J, Fang S S, Han W X, Li J Y, Du Y B, Ming J X, Zhang T S, Zhang J, Kang J, Li X Y, Xu W G, Chen Y B 2025 Nat. Commun. 16 4901

[73] Wieting T J 1973 Solid State Commun. 12 931

[74] Xie X, Ding J N, Wu B, Zheng H H, Li S F, He J, Liu Z W, Wang J T, Liu Y P 2023 Phys. Rev. B 108 155302

[75] Liang L B, Zhang J, Sumpter B G, Tan Q H, Tan P H, Meunier V 2017 ACS Nano 11 11777

[76] Zhao Y Y, Luo X, Li H, Zhang J, Araujo P T, Gan C K, Wu J, Zhang H, Quek S Y, Dresselhaus M S, Xiong Q H 2013 Nano Lett. 13 1007

[77] Dong J S, Ouyang G 2020 Chin. Phys. B 29 086403

[78] Han B, Li F F, Li L, Huang X L, Gong Y B, Fu X P, Gao H X, Zhou Q, Cui T 2017 J. Phys. Chem. Lett. 8 941

[79] Chi Z H, Chen X L, Yen F, Peng F, Zhou Y H, Zhu J L, Zhang Y J, Liu X D, Lin C L, Chu S Q, Li Y C, Zhao J G, Kagayama T, Ma Y M, Yang Z R 2018 Phys. Rev. Lett. 120 037002

[80] Zhao W J, Ghorannevis Z, Chu L Q, Toh M L, Kloc C, Tan P H, Eda G 2013 ACS Nano 7 791

[81] Pandey S K, Das R, Mahadevan P 2020 ACS Omega 5 15169

[82] Fan X, Chang C H, Zheng W T, Kuo J L, Singh D J 2015 J. Phys. Chem. C 119 10189

[83] Kuc A, Zibouche N, Heine T 2011 Phys. Rev. B 83 245213

[84] Bussolotti F, Kawai H, Ooi Z E, Chellappan V, Thian D, Pang A L C, Goh K E J 2018 Nano Futures 2 032001

[85] Ye Y X, Dou X M, Ding K, Jiang D S, Yang F H, Sun B Q 2016 Nanoscale 8 10843

[86] Fu X P, Li F F, Lin J F, Gong Y B, Huang X L, Huang Y P, Han B, Zhou Q, Cui T 2017 J. Phys. Chem. Lett. 8 3556

[87] Pimenta Martins L G, Carvalho B R, Occhialini C A, Neme N P, Park J H, Song Q, Venezuela P, Mazzoni M S C, Matos M J S, Kong J, Comin R 2022 ACS Nano 16 8064

[88] Qiao W, Sun H, Fan X Y, Jin M L, Liu H Y, Tang T H, Xiong L, Niu B H, Li X, Wang G 2022 Crystals 12 693 DOI:

[89] Li Q Y, Sui L Z, Niu G M, Jiang J T, Zhang Y T, Wu G R, Jin M X, Yuan K J 2020 J. Phys. Chem. C 124 11183

[90] Dou X M, Ding K, Jiang D S, Fan X F, Sun B Q 2016 ACS Nano 10 1619

[91] Hsu W T, Quan J, Pan C R, Chen P J, Chou M Y, Chang W H, MacDonald A H, Li X, Lin J F, Shih C K 2022 Phys. Rev. B 106 125302

[92] Steeger P, Graalmann J H, Schmidt R, Kupenko I, Sanchez-Valle C, Marauhn P, Deilmann T, de Vasconcellos S M, Rohlfing M, Bratschitsch R 2023 Nano Lett. 23 8947

[93] Bai Z Y, Zhang H, He J Q, He D W, Wang J R, Li G L, Bai J X, Zhao K, Yu X H, Wang Y S, Zhang X X 2023 Nano Res. 16 12738

[94] Chen Y B, Ke F, Ci P H, Ko C, Park T, Saremi S, Liu H L, Lee Y, Suh J, Martin L W, Ager J W, Chen B, Wu J Q 2017 Nano Lett. 17 194

[95] Qin X X, Zhang G Z, Chen L, Wang Q L, Wang G Y, Zhang H W, Li Y W, Liu C L 2024 Ultrafast Sci. 4 0044

[96] Tu H Y, Pan L Y, Qi H J, Zhang S H, Li F F, Sun C L, Wang X, Cui T 2023 J. Phys. : Condens. Matter 35 253002

[97] Bai Z, Zhang H, He J, He D, Wang J, Wu W, Zhang Y, Wang W, Wang Y, Yu X, Zhang X 2025 Adv. Electron. Mater. 11 2400333

[98] Li Z Y, Qin F, Ong C S, Huang J W, Xu Z A, Chen P, Qiu C Y, Zhang X, Zhang C R, Zhang X X, Eriksson O, Rubio A, Tang P Z, Yuan H T 2023 Nano Lett. 23 10282

[99] Fu X P, Li F F, Lin J F, Gong Y B, Huang X L, Huang Y P, Gao H X, Zhou Q, Cui T 2018 J. Phys. Chem. C 122 5820 DOI:

[100] Yan W, Meng L, Meng Z S, Weng Y K, Kang L L, Li X A 2019 J. Phys. Chem. C 123 30684

[101] Villafañe V, Kremser M, Hübner R, Petrić M M, Wilson N P, Stier A V, Müller K, Florian M, Steinhoff A, Finley J J 2023 Phys. Rev. Lett. 130 026901

[102] uang S, Liang L, Ling X, Puretzky A A, Geohegan D B, Sumpter B G, Kong J, Meunier V, Dresselhaus M S 2016 Nano Lett. 16 1435

[103] Puretzky A A, Liang L, Li X, Xiao K, Sumpter B G, Meunier V, Geohegan D B 2016 ACS Nano 10 2736

[104] Fan W, Zhu X, Ke F, Chen Y, Dong K, Ji J, Chen B, Tongay S, Ager J W, Liu K, Su H, Wu J 2015 Phys. Rev. B 92 241408

[105] Xie X, Ding J, Wu B, Zheng H, Li S, Wang C T, He J, Liu Z, Wang J T, Liu Y 2023 Nano Lett. 23 8833

[106] Jiao C, Pei S, Zhang Z, Li C, Zhu J, Qin J, Zhang M, Wen T, Zhou Y, Wang Z, Xia J 2024 Appl. Phys. Rev. 11 031417

[107] Zhang Z, Jiao C, Pei S, Zhou X, Qin J, Zhang W, Zhou Y, Wang Z, Xia J 2024 Sci. China: Phys., Mech. Astron. 67 288211

[108] Li C, Cheng W, Zhang X, Zhang P, Zheng Q, Yan Z, Han J, Dai G, Wang S, Quan Z, Liu Y, Zhu J 2023 J. Phys. Chem. C 127 7784

[109] Yan Y, Feng D, Zhu J, Li F 2025 J. Alloys Compd. 1014 178651

[110] Li S, Zheng H, Ding J, Wu B, He J, Liu Z, Liu Y 2022 Nano Res. 15 7688

[111] Xia J, Yan J, Wang Z, He Y, Gong Y, Chen W, Sum T C, Liu Z, Ajayan P M, Shen Z 2021 Nat. Phys. 17 92

[112] Kang J, Tongay S, Zhou J, Li J, Wu J 2013 Appl. Phys. Lett. 102 012111

[113] Tebyetekerwa M, Zhang J, Saji S E, Wibowo A A, Rahman S, Truong T N, Lu Y, Yin Z, Macdonald D, Nguyen H T 2021 Cell Rep. Phys. Sci. 2 100509

[114] Alexeev E M, Ruiz-Tijerina D A, Danovich M, Hamer M J, Terry D J, Nayak P K, Ahn S, Pak S, Lee J, Sohn J I, Molas M R, Koperski M, Watanabe K, Taniguchi T, Novoselov K S, Gorbachev R V, Shin H S, Fal'ko V I, Tartakovskii A I 2019 Nature 567 81

[115] Kunstmann J, Mooshammer F, Nagler P, Chaves A, Stein F, Paradiso N, Plechinger G, Strunk C, Schüller C, Seifert G, Reichman D R, Korn T 2018 Nat. Phys. 14 801

[116] Li Y, Song Z 2023 J. Phys. : Conf. Ser. 2566 012105

[117] Zhu M, Zhang Z, Zhang T, Liu D, Zhang H, Zhang Z, Li Z, Cheng Y, Huang W 2022 Nano Lett. 22 4528

[118] Ma X, Fu S, Ding J, Liu M, Bian A, Hong F, Sun J, Zhang X, Yu X, He D 2021 Nano Lett. 21 8035

[119] Miller B, Steinhoff A, Pano B, Klein J, Jahnke F, Holleitner A, Wurstbauer U 2017 Nano Lett. 17 5229

[120] Jiang C, Xu W, Rasmita A, Huang Z, Li K, Xiong Q, Gao W-B 2018 Nat. Commun. 9 753

[121] Zhang W, Wang Q, Chen Y, Wang Z, Wee A T S 2016 2D Mater. 3 022001 DOI:

[122] Gong Y, Lin J, Wang X, Shi G, Lei S, Lin Z, Zou X, Ye G, Vajtai R, Yakobson B I, Terrones H, Terrones M, Tay Beng K, Lou J, Pantelides S T, Liu Z, Zhou W, Ajayan P M 2014 Nat. Mater. 13 1135

[123] Rivera P, Schaibley J R, Jones A M, Ross J S, Wu S, Aivazian G, Klement P, Seyler K, Clark G, Ghimire N J, Yan J, Mandrus D G, Yao W, Xu X 2015 Nat. Commun. 6 6242

[124] Choudhary N, Park J, Hwang J Y, Chung H S, Dumas K H, Khondaker S I, Choi W, Jung Y 2016 Sci. Rep. 6 25456

[125] Jiang Y, Chen S, Zheng W, Zheng B, Pan A 2021 Light: Sci. Appl. 10 72

[126] Zhang Z, Wang Y, Watanabe K, Taniguchi T, Ueno K, Tutuc E, LeRoy B J 2020 Nat. Phys. 16 1093

[127] Li H, Li S, Naik M H, Xie J, Li X, Wang J, Regan E, Wang D, Zhao W, Zhao S, Kahn S, Yumigeta K, Blei M, Taniguchi T, Watanabe K, Tongay S, Zettl A, Louie S G, Wang F, Crommie M F 2021 Nat. Mater. 20 945

[128] Zhang C, Chuu C P, Ren X, Li M Y, Li L J, Jin C, Chou M Y, Shih C K 2017 Sci. Adv. 3 e1601459

[129] Tran K, Moody G, Wu F, Lu X, Choi J, Kim K, Rai A, Sanchez D A, Quan J, Singh A, Embley J, Zepeda A, Campbell M, Autry T, Taniguchi T, Watanabe K, Lu N, Banerjee S K, Silverman K L, Kim S, Tutuc E, Yang L, MacDonald A H, Li X 2019 Nature 567 71

[130] Baek H, Brotons-Gisbert M, Koong Z X, Campbell A, Rambach M, Watanabe K, Taniguchi T, Gerardot B D 2020 Sci. Adv. 6 eaba8526

[131] Soltero I, Kaliteevski M A, McHugh J G, Enaldiev V, Fal'ko V I 2024 Nano Lett. 24 1996

[132] Pimenta Martins L G, Ruiz-Tijerina D A, Occhialini C A, Park J H, Song Q, Lu A Y,

Venezuela P, Cançado L G, Mazzoni M S C, Matos M J S, Kong J, Comin R 2023 Nat. Nanotechnol. 18 1147

[133] Enaldiev V V, Ferreira F, Magorrian S J, Fal'ko V I 2021 2D Mater. 8 025030

[134] Xie X, Chen J Y, Li S F, Ding J N, He J, Liu Z W, Wang J T, Liu Y P 2025 Nano Lett. 25 8571

[135] Zhao W Y, Regan E C, Wang D, Jin C, Hsieh S, Wang Z L, Wang J L, Wang Z, Yumigeta K, Blei M, Watanabe K, Taniguchi T, Tongay S, Yao N Y, Wang F 2021 Nano Lett. 21 8910

[136] Jo S, Costanzo D, Berger H, Morpurgo A F 2015 Nano Lett. 15 1197

[137] Shi W, Ye J T, Zhang Y J, Suzuki R, Yoshida M, Miyazaki J, Inoue N, Saito Y, Iwasa Y 2015 Sci. Rep. 5 12534

[138] Ye J T, Zhang Y J, Akashi R, Bahramy M S, Arita R, Iwasa Y 2012 Science 338 1193

[139] Ding D D, Qu Z Z, Han X Y, Han C R, Zhuang Q, Yu X L, Niu R R, Wang Z Y, Li Z X, Gan Z, Wu J S, Lu J M 2022 Nano Lett. 22 7919

[140] Piatti E, De Fazio D, Daghero D, Tamalampudi S R, Yoon D, Ferrari A C, Gonnelli R S 2018 Nano Lett. 18 4821

[141] Wang L, Shih E M, Ghiotto A, Xian L D, Rhodes D A, Tan C, Claassen M, Kennes D M, Bai Y, Kim B, Watanabe K, Taniguchi T, Zhu X, Hone J, Rubio A, Pasupathy A N, Dean C R 2020 Nat. Mater. 19 861

[142] Huang X, Wang T M, Miao S N, Wang C, Li Z P, Lian Z, Taniguchi T, Watanabe K, Okamoto S, Xiao D, Shi S F, Cui Y T 2021 Nat. Phys. 17 715

[143] Xiong R C, Nie J H, Brantly S L, Hays P, Sailus R, Watanabe K, Taniguchi T, Tongay S, Jin C H 2023 Science 380 860

[144] Bai Y, Li Y, Liu S, Guo Y, Pack J, Wang J, Dean C R, Hone J, Zhu X 2023 Nano Lett. 23 11621

[145] Wang Z F, Rhodes D A, Watanabe K, Taniguchi T, Hone J C, Shan J, Mak K F 2019 Nature 574 76

[146] Nguyen P X, Ma L G, Chaturvedi R, Watanabe K, Taniguchi T, Shan J, Mak K F 2025 Science 388 274

[147] Gao Y F, Xu Q L, Farooq M U, Xian L D, Huang L 2023 Nano Lett. 23 7921

[148] Brzezińska M, Grytsiuk S, Rösner M, Gibertini M, Rademaker L 2025 2D Mater. 12 015003

[149] Arovas D P, Berg E, Kivelson S A, Raghu S 2022 Annu. Rev. Condens. Matter Phys. 13 239

[150] Giuliani A, Mastropietro V 2010 Commun. Math. Phys. 293 301